Monthly Notices
of the
ROYAL ASTRONOMICAL SOCIETY

MNRAS **445,** 479–499 (2014) doi:10.1093/mnras/stu1715

On the formation of planetary systems via oligarchic growth in thermally evolving viscous discs

Gavin A. L. Coleman★ and Richard P. Nelson

Astronomy Unit, Queen Mary University of London, Mile End Road, London E1 4NS, UK

Accepted 2014 August 20. Received 2014 August 20; in original form 2014 June 9

ABSTRACT

We present *N*-body simulations of planetary system formation in thermally evolving, viscous disc models. The simulations incorporate type I migration (including corotation torques and their saturation), gap formation, type II migration, gas accretion on to planetary cores and gas disc dispersal through photoevaporation. The aim is to examine whether or not the oligarchic growth scenario, when combined with self-consistent disc models and up-to-date prescriptions for disc-driven migration, can produce planetary systems similar to those that have been observed. The results correlate with the initial disc mass. Low-mass discs form close-packed systems of terrestrial-mass planets and super-Earths. Higher mass discs form multiple generations of planets, with masses in the range $10 \lesssim m_{\rm p} \lesssim 45\,{\rm M}_{\oplus}$. These planets generally type I migrate into the inner disc, because of corotation torque saturation, where they open gaps and type II migrate into the central star. Occasionally, a final generation of low- to intermediate-mass planets forms and survives due to gas disc dispersal. No surviving gas giants were formed in our simulations. Analysis shows that these planets can only survive migration if a core forms and experiences runaway gas accretion at orbital radii $r \gtrsim 10$ au prior to the onset of type II migration. We conclude that planet growth above masses $m_{\rm p} \gtrsim 10\,{\rm M}_{\oplus}$ during the gas disc lifetime leads to corotation torque saturation and rapid inward migration, preventing the formation and survival of gas giants. This result is in contrast to the success in forming gas giant planets displayed by some population synthesis models. This discrepancy arises, in part, because the type II migration prescription adopted in the population synthesis models causes too large a reduction in the migration speed when in the planet-dominated regime.

Key words: planets and satellites: formation – planet–disc interactions – protoplanetary discs – planetary systems.

1 INTRODUCTION

With the number of confirmed exoplanets now exceeding 1700 (www.exoplanets.eu, Schneider et al. 2011), the full diversity of extrasolar planetary systems is starting to be revealed. The known systems now include numerous short-period hot planets with a range of masses, such as 51 Pegasi (Mayor & Queloz 1995), Kepler-10b (Batalha et al. 2011) and Wasp-103b (Gillon et al. 2014). At the other end of the spectrum, there exist systems of long-period massive giant planets, detected through direct imaging, such as HR 8799b-d (Soummer et al. 2011). Among the more exotic and dynamically interesting systems to be discovered are the short-period compact systems comprising low-mass planets, such as Kepler-11 (Lissauer et al. 2011). Key questions that need to be addressed are whether or not a particular model of planetary formation, involving common physical processes, can explain this broad diversity, or whether it is necessary to invoke different formation scenarios for systems with very different architectures. For example, one might invoke the core accretion scenario to explain the lower mass planets found to be orbiting with short periods (Pollack et al. 1996; Hubickyj, Bodenheimer & Lissauer 2005), and gravitational instability during the early lifetime of a massive protoplanetary disc to explain the systems with long-period gas giant planets (Boss 1997; Forgan & Rice 2013). The primary aim of this work is to examine the types of planetary systems that emerge from the oligarchic growth of planetary embryos embedded in a gaseous protoplanetary disc, using the most up-to-date descriptions of migration and other processes such as gas accretion on to planetary cores. In the classical theory of planet formation, the emergence of km-sized planetesimals leads to a period of *runaway growth*, during which the most massive planetesimals undergo rapid, gravity-assisted accretion from

★ E-mail: g.coleman@qmul.ac.uk

the surrounding planetesimal swarm to form planetary embryos. Runaway growth transitions to oligarchic growth when the velocity dispersion in the swarm becomes dominated by perturbations induced by the embryos (or oligarchs), and it is during this phase of evolution that we initiate our simulations. Our approach is to utilize *N*-body simulations coupled with self-consistent 1D models of thermally evolving viscous protoplanetary discs that are subject to photoevaporation over Myr time-scales. These disc models also allow gap formation and migration of more massive planets to be treated in a self-consistent manner. A particular focus of this study is the influence of corotation torques on the migration behaviour of growing protoplanets.

A large body of related work that has used *N*-body simulations to examine planet formation, in the presence of a gas disc, has been published in recent years. For example, Papaloizou & Larwood (2000) examined planetary growth through planet–planet collisions using *N*-body simulations combined with models for migration and eccentricity/inclination damping. McNeil, Duncan & Levison (2005) and Daisaka, Tanaka & Ida (2006) examined the effects of type I migration on terrestrial planet formation. Fogg & Nelson (2007, 2009) examined the influence of type I migration on the formation of terrestrial planets in the presence of migrating Jovian-mass planets. Terquem & Papaloizou (2007) examined the formation of hot super-Earths and Neptunes using *N*-body simulations combined with a prescription for type I migration, and a disc model that included an inner cavity created by the stellar magnetosphere. McNeil & Nelson (2009, 2010) performed large-scale simulations of oligarchic growth to examine the formation of systems containing multiple super-Earths and Neptune-mass planets, such as Gliese 581 and HD 69830. More recently, Hellary & Nelson (2012) examined the influence of disc-induced corotation torques experienced by low-mass planets on the formation of planetary systems, using simple disc models with power-law surface and temperature profiles. Cossou, Raymond & Pierens (2013) have examined how planet convergence zones, generated by the combined action of outwardly directed corotation torques and inwardly directed Lindblad torques, are shifted in multiple planet systems by the influence of orbital eccentricity on the strength of the corotation torque. In follow-on work, Pierens, Cossou & Raymond (2013) have examined how corotation torques can assist in the formation of giant planet cores.

An alternative approach to simulating planet formation using *N*-body simulations has been planetary population synthesis modelling, as exemplified by Ida & Lin (2010), Ida, Lin & Nagasawa (2013), Mordasini, Alibert & Benz (2009), Mordasini et al. (2012) and Miguel, Guilera & Brunini (2011a,b). These Monte Carlo approaches have the advantage of computational speed over *N*-body simulations, enabling coverage of large areas of parameter space, hence allowing statistical comparisons to be made with observations. Computational efficiency also allows sophisticated models of gaseous envelope accretion to be incorporated (e.g. Mordasini et al. 2009). One significant disadvantage associated with these Monte Carlo approaches is that planet–planet interactions are generally neglected, although recent work has started to address this issue (Ida & Lin 2010; Alibert et al. 2013). The medium-term trajectory of this subject area is clearly towards convergence between the population synthesis and full *N*-body approaches.

To begin answering the question of how observed exoplanetary systems form, global models of planet formation that allow the formation and evolution of these systems over a large range of orbital length-scales need to be constructed. In this paper, we present the results of simulations of oligarchic growth, performed using the MERCURY-6 symplectic integrator (Chambers 1999) that computes the dynamical evolution and collisional accretion of a system of planetary embryos and planetesimals. This is combined with a 1D viscous disc model that incorporates thermal evolution through stellar irradiation, viscous dissipation and blackbody cooling. The migration of low-mass planets is modelled through implementation of the torque prescriptions given by Paardekooper, Baruteau & Kley (2011), including the effects of corotation torque saturation. Gap formation and type II migration of gap forming planets is modelled self-consistently using the impulse-approximation approach first introduced by Lin & Papaloizou (1986). The simulations also incorporate models for gas envelope accretion, enhanced planetesimal capture by planetary atmospheres and gas disc dispersal through photoevaporation over Myr time-scales. We explore a range of model parameters including disc mass, metallicity and planetesimal radii to examine their influence on the types of planetary systems that emerge. One of our main results is that the scenario under investigation has severe difficulty in accounting for the observed gas giant planets orbiting at a range of radii, because migration delivers them and their moderate-mass precursors into the central star on time-scales that are shorter than the gas disc dispersal time-scale. The model is successful in forming a diversity of low- and intermediate-mass planets that range in mass from sub-Earth mass up to $\sim$ Neptune mass, but in general these are significantly less compact than the systems of super-Earths and Neptunes that have been discovered in recent years.

The paper is organized as follows. We present the physical model and numerical methods in Section 2, and our simulation results in Section 3. The results are compared with observations in Section 4. We present an analysis of the conditions required for giant planet survival in Section 5, and in Section 6 we draw our conclusions.

2 PHYSICAL MODEL AND NUMERICAL METHODS

In the following sections, we provide details of the physical model we adopt and the numerical scheme used to undertake the simulations. The basic model consists of a few tens of protoplanets, embedded in a swarm of thousands of planetesimals, embedded in a gaseous protoplanetary disc, all orbiting around a solar-mass star.

2.1 Disc model

We adopt a 1D viscous disc model for which the equilibrium temperature at each time step is calculated by balancing irradiation heating by the central star, viscous heating and blackbody cooling. The disc surface density, Σ, is evolved by solving the standard diffusion equation

$$\frac{\mathrm{d}\Sigma}{\mathrm{d}t} = \frac{1}{r}\frac{\mathrm{d}}{\mathrm{d}r}\left[3r^{1/2}\frac{\mathrm{d}}{\mathrm{d}r}(\nu\Sigma r^{1/2}) - \frac{2\Lambda\Sigma r^{3/2}}{GM_*}\right] - \frac{\mathrm{d}\Sigma_\mathrm{w}}{\mathrm{d}t}, \quad (1)$$

where $\mathrm{d}\Sigma_\mathrm{w}/\mathrm{d}t$ is the rate of change in surface density due to the photoevaporative wind, and Λ is the disc–planet torque that operates when a planet becomes massive enough to open a gap in the disc. An explicit finite difference scheme is used to solve equation (1), and a non-uniform mesh is adopted, for which the grid spacing scales with radius according to $\Delta r \propto r$. The inner boundary condition mimics accretion on to the star through gas removal by setting $\Sigma_\mathrm{g}(1) = 0.99 \times \Sigma_\mathrm{g}(2)$. The outer boundary condition sets the radial velocity to zero. 1000 grid cells were used in the calculations.

The disc–planet torque per unit mass that applies for planets whose masses are large enough to open gaps is given by

$$\Lambda = \mathrm{sign}(r - r_\mathrm{p}) q^2 \frac{GM_*}{2r} \left(\frac{r}{|\Delta_\mathrm{p}|} \right)^4, \quad (2)$$

where q is the planet/star mass ratio, r_p is the planet orbital radius and $|\Delta_\mathrm{p}| = \max(H, |r - r_\mathrm{p}|)$. H is the local disc scaleheight. We use the standard α model for the disc viscosity (Shakura & Sunyaev 1973)

$$\nu = \alpha c_\mathrm{s}^2 / \Omega, \quad (3)$$

where c_s is the local sound speed, Ω is the angular velocity and α is the viscosity parameter, taken to be $\alpha = 2 \times 10^{-3}$ in this work. The gas surface density profile is initialized according to

$$\Sigma_\mathrm{g}(r) = \Sigma_\mathrm{g}(1\,\mathrm{au}) \left(\frac{r}{1\,\mathrm{au}} \right)^{-1.5}, \quad (4)$$

where $\Sigma_\mathrm{g}(1\,\mathrm{au})$ is used to normalize the total disc mass. The temperature profile is initialized as a power-law function of radius with index -0.5. During the simulations, the temperature is obtained by using an iterative method to solve the following equation for thermal equilibrium

$$Q_\mathrm{irr} + Q_\nu - Q_\mathrm{cool} = 0, \quad (5)$$

where Q_ν is the viscous heating rate per unit area of the disc, Q_irr is the radiative heating rate due to the central star and Q_cool is the radiative cooling rate. For a Keplerian disc, we have

$$Q_\nu = \frac{9}{4} \nu \Sigma \Omega^2. \quad (6)$$

The heating rate due to stellar irradiation is given by

$$Q_\mathrm{irr} = 2\sigma T_\mathrm{irr}^4 \left(\frac{3}{8}\tau_\mathrm{R} + \frac{1}{2} + \frac{1}{4\tau_\mathrm{p}} \right)^{-1}, \quad (7)$$

where T_irr is given by Menou & Goodman (2004),

$$T_\mathrm{irr}^4 = \left(T_\mathrm{S}^4 + T_\mathrm{acc}^4 \right) (1 - \epsilon) \left(\frac{R_\mathrm{S}}{r} \right)^2 W_\mathrm{G}. \quad (8)$$

Here, ϵ is the disc albedo (taken to be 0.5), τ_R and τ_p are the optical depths due to the Rosseland and Planck mean opacities, respectively (assumed to be equivalent in this work), T_acc is the contribution made to the irradiation temperature by accretion of gas on to the star and W_G is a geometrical factor that determines the flux of radiation that is intercepted by the disc surface. This approximates to

$$W_\mathrm{G} = 0.4 \left(\frac{R_\mathrm{S}}{r} \right) + \frac{2}{7} \frac{H}{r} \quad (9)$$

as given by D'Angelo & Marzari (2012). Quantities with a subscript 'S' are the values for the central star.

For disc cooling, we adopt the equation given by Hubeny (1990):

$$Q_\mathrm{cool} = 2\sigma T^4 \left(\frac{3}{8}\tau_\mathrm{R} + \frac{1}{2} + \frac{1}{4\tau_\mathrm{p}} \right)^{-1}, \quad (10)$$

where σ is the Stefan–Boltzmann constant and T is the temperature of the disc mid-plane.

2.2 Photoevaporation

The absorption of UV radiation from the star by the disc can heat the disc above the local escape velocity, and hence drive a photoevaporative wind. Ultimately this photoevaporative wind is responsible for removing the final remnants of the gaseous protoplanetary disc.

Table 1. Disc model parameters.

Parameter	Value
Disc inner boundary	0.1 au
Disc outer boundary	40 au
Number of cells	1000
$\Sigma_\mathrm{g}(1\,\mathrm{au})$	1731 g cm^{-2}
Stellar mass	1 M$_\odot$
R_S	2 R$_\odot$
T_S	4280 K
f_{41}	10

We adopt the formula provided by Dullemond et al. (2007) to calculate the rate at which the surface density decreases due to this wind:

$$\frac{\mathrm{d}\Sigma_\mathrm{w}}{\mathrm{d}t} = 1.16 \times 10^{-11} G_\mathrm{fact} \sqrt{f_{41}} \left(\frac{1}{r - r_g} \right)^{3/2} \left(\frac{\mathrm{M}_\odot}{\mathrm{au}^2\,\mathrm{yr}} \right), \quad (11)$$

where G_fact is a scaling factor defined as

$$G_\mathrm{fact} = \begin{cases} \left(\frac{r_\mathrm{g}}{r}\right)^2 e^{(1/2)\left(1 - \frac{r_\mathrm{g}}{r}\right)} & r \leq (r - r_\mathrm{g}), \\ \left(\frac{r_\mathrm{g}}{r}\right)^{5/2} & r > (r - r_\mathrm{g}). \end{cases} \quad (12)$$

Here, r_g is the characteristic radius beyond which gas becomes unbound from the system, which is set to 10 au in our simulations, and f_{41} is the rate at which extreme UV ionizing photons are emitted by the central star in units of 10^{41} s^{-1}.

2.3 Opacities

We take the opacity, κ, to be equal to the Rosseland mean opacity, with the temperature and density dependences calculated using the formulae in Bell et al. (1997) for temperatures below 3730 K, and by Bell & Lin (1994) above 3730 K:

$$\kappa[\mathrm{cm}^2\,\mathrm{g}^{-1}] = \begin{cases} 10^{-4} T^{2.1} & T < 132\,\mathrm{K} \\ 3T^{-0.01} & 132 \leq T < 170\,\mathrm{K} \\ T^{-1.1} & 170 \leq T < 375\,\mathrm{K} \\ 5 \times 10^4 T^{-1.5} & 375 \leq T < 390\,\mathrm{K} \\ 0.1 T^{0.7} & 390 \leq T < 580\,\mathrm{K} \\ 2 \times 10^{15} T^{-5.2} & 580 \leq T < 680\,\mathrm{K} \\ 0.02 T^{0.8} & 680 \leq T < 960\,\mathrm{K} \\ 2 \times 10^{81} \rho T^{-24} & 960 \leq T < 1570\,\mathrm{K} \\ 10^{-8} \rho^{2/3} T^3 & 1570 \leq T < 3730\,\mathrm{K} \\ 10^{-36} \rho^{1/3} T^{10} & 3730 \leq T < 10\,000\,\mathrm{K} \end{cases}. \quad (13)$$

To account for changes in the disc metallicity, we multiply the opacity by the metallicity relative to solar given in our initial conditions. We assume that the metallicity, dust size and the solid/gas ratio remain constant throughout the simulations. A summary of the parameters adopted is given in Table 1.

2.4 Aerodynamic drag

Planetesimals experience aerodynamic drag, which can damp eccentricities and inclinations while simultaneously reducing planetesimal semimajor axes. We apply gas drag to planetesimals using the Stokes' drag law (Adachi, Hayashi & Nakazawa 1976)

$$\boldsymbol{F}_\mathrm{drag} = m_\mathrm{pl} \left(\frac{-3\rho C_\mathrm{D}}{9\rho_\mathrm{pl} R_\mathrm{pl}} \right) v_\mathrm{rel} \boldsymbol{v}_\mathrm{rel}. \quad (14)$$

Here, a subscript 'pl' corresponds to planetesimals, ρ is the local gas density, $\rho_{\rm pl}$ is the internal density of planetesimals, $R_{\rm pl}$ is the planetesimal radius, $C_{\rm D}$ is the dimensionless drag coefficient (here taken to be unity) and $v_{\rm rel}$ is the relative velocity between the gas and planetesimals.

2.5 Type I migration

Planets with masses that significantly exceed the lunar mass undergo migration through gravitational interaction with the surrounding disc. In our simulations, we implement the torque formulae presented by Paardekooper et al. (2010, 2011). These formulae take into account how planet masses, and changes in local disc conditions, modify the various torque contributions for the planet. Corotation torques are especially sensitive to the ratio of the horseshoe libration time-scale to either the viscous or thermal diffusion time-scales across the horseshoe region.

By using equations 50–53 in Paardekooper et al. (2011), we obtain an expression giving the total type I torque acting on a planet as

$$\Gamma_{\rm I,tot} = F_{\rm L}\Gamma_{\rm LR} + \Big\{\Gamma_{\rm VHS}F_{p_v}G_{p_v} + \Gamma_{\rm EHS}F_{p_v}F_{p_\chi}\sqrt{G_{p_v}Gp_\chi} + \Gamma_{\rm LVCT}(1-K_{p_v}) + \Gamma_{\rm LECT}\sqrt{(1-K_{p_v})(1-K_{p_\chi})}\Big\}F_eF_i, \quad (15)$$

where $\Gamma_{\rm LR}$, $\Gamma_{\rm VHS}$, $\Gamma_{\rm EHS}$, $\Gamma_{\rm LVCT}$ and $\Gamma_{\rm LECT}$ are the Lindblad torque, vorticity and entropy-related horseshoe drag torques, and linear vorticity and entropy-related corotation torques, respectively, as given by equations 3–7 in Paardekooper et al. (2011). The functions F_{p_v}, F_{p_χ}, G_{p_v}, G_{p_χ}, K_{p_v} and K_{p_χ} are related to the ratio between viscous/thermal diffusion time-scales and horseshoe libration/horseshoe U-turn time-scales, as given by equations 23, 30 and 31 in Paardekooper et al. (2011). Changes in local disc conditions brought about by changes in temperature, surface density and metallicity/opacity can alter the magnitude of the functions given in Paardekooper et al. (2011), and thus the magnitude and possibly the direction of the torque calculated in equation (15). The factors F_e and F_i, multiplying all terms relating to the corotation torque, allow for the fact that a planet's eccentricity and inclination can attenuate the corotation torque (Bitsch & Kley 2010). To account for the effect of eccentricity, we use the formula suggested by Fendyke & Nelson (2014):

$$F_e = \exp\left(-\frac{e}{e_f}\right), \quad (16)$$

where e is the planet's eccentricity and e_f is defined as

$$e_f = h/2 + 0.01 \quad (17)$$

where h is the disc aspect ratio at the planet's location. It should be noted that these formulae differ from the one suggested originally by Hellary & Nelson (2012), who argued that the quantity that controls the decrease in the corotation torque as a planet's orbit becomes eccentric should be the ratio of the eccentricity and the dimensionless horseshoe width. The analysis presented by Fendyke & Nelson (2014) indicates that the quantity controlling the decrease in corotation torque is e/h instead. In general, equation (16) results in a slower attenuation of the corotation torque with increasing eccentricity than the formula adopted by Hellary & Nelson (2012). To account for the effect of orbital inclination, we define F_i as

$$F_i = 1 - \tanh(i/h), \quad (18)$$

where i is the inclination of the planet.

The factor $F_{\rm L}$ in equation (15) accounts for the reduction in Lindblad torques when planets are on eccentric or inclined orbits, and is given by Cresswell & Nelson (2008) as

$$F_{\rm L} = \left[P_e + \left(\frac{P_e}{|P_e|}\right)\times\left\{0.07\left(\frac{i}{h}\right) + 0.085\left(\frac{i}{h}\right)^4 - 0.08\left(\frac{e}{h}\right)\left(\frac{i}{h}\right)^2\right\}\right]^{-1}, \quad (19)$$

where P_e is defined as

$$P_e = \frac{1+\left(\frac{e}{2.25h}\right)^{1/2}+\left(\frac{e}{2.84h}\right)^6}{1-\left(\frac{e}{2.02h}\right)^4}. \quad (20)$$

2.5.1 Eccentricity and inclination damping

To damp protoplanet eccentricities, we use a simple time-scale damping formula given as

$$F_{\rm edamp,r} = -\frac{v_r}{t_{\rm edamp}}, \quad F_{{\rm edamp},\theta} = -\frac{-0.5(v_\theta - v_K)}{t_{\rm edamp}}, \quad (21)$$

where

$$t_{\rm edamp} = \frac{t_{\rm wave}}{0.78}\times\left[1 - 0.14\left(\frac{e}{h}\right)^2 + 0.06\left(\frac{e}{h}\right)^3 + 0.18\left(\frac{e}{h}\right)\left(\frac{i}{h}\right)^2\right], \quad (22)$$

where $t_{\rm wave}$ is specified as

$$t_{\rm wave} = \left(\frac{m_{\rm p}}{{\rm M}_\odot}\right)^{-1}\left(\frac{a_{\rm p}\Omega_{\rm p}}{c_{\rm s}}\right)^{-4}\left(\frac{\Sigma_{\rm p}a_{\rm p}^2}{{\rm M}_\odot}\right)^{-1}\Omega_{\rm p}^{-1}. \quad (23)$$

We damp inclinations using the prescription given in Daisaka et al. (2006), as adapted by Cresswell & Nelson (2008):

$$F_{{\rm idamp},z} = \frac{0.544}{t_{\rm wave}}(2A_{cz}v_z + A_{sz}z\Omega_{\rm p})\times\left[1 - 0.3\left(\frac{i}{h}\right)^2 + 0.24\left(\frac{i}{h}\right)^3 + 0.14\left(\frac{i}{h}\right)\left(\frac{e}{h}\right)^2\right]^{-1}, \quad (24)$$

where $A_{cz} = -1.088$ and $A_{sz} = -0.871$.

2.6 Type II migration

Once a planet becomes massive enough to form a gap in a disc, its migration changes from type I to type II. We implement this transition by allowing the planet torque term in equation (1) to act on the disc and open a gap only when $R_{\rm H} > 3H/4$, where $R_{\rm H}$ is the planet's Hill radius.[1] The type II migration torque per unit mass is then given by

$$\Gamma_{\rm II} = -\frac{2\pi}{m_{\rm p}}\int_{r_{\rm in}}^{r_{\rm out}} r\Lambda\Sigma_{\rm g}{\rm d}r. \quad (25)$$

[1] Our intention was to use the gap formation criterion $\frac{3H}{4R_{\rm H}} + \frac{50\nu}{qr_{\rm p}^2\Omega_{\rm p}} \leq 1$ from Crida, Morbidelli & Masset (2006). A typographical error in our code led to the term involving the viscosity ν being evaluated to zero in all runs. We have verified that when our code transitions to type II migration according to the gap formation criterion described in the main text, our disc model does indeed respond by beginning to form a gap.

We transition smoothly between type I and type II migration by using the expression

$$\Gamma_{\rm eff} = \Gamma_{\rm II} B + \Gamma_{\rm I}(1 - B), \tag{26}$$

where $\Gamma_{\rm eff}$ is the torque applied during the transition, $\Gamma_{\rm I}$ is the type I torque and $\Gamma_{\rm II}$ is the type II torque as given above The transition function, B, is given by

$$B = 0.5 + 0.5 \tanh\left(\frac{m_{\rm p} - m_{\rm switch}}{1.5\,{\rm M}_{\oplus}}\right), \tag{27}$$

where $m_{\rm switch}$ is the planet mass that corresponds to the gap opening criterion described above. When a planet is in the type II regime, the eccentricities and inclinations are damped on a time-scale that is equal to 10 local orbit periods.

2.7 Gas envelope accretion

Once a protoplanet grows through mutual collisions and planetesimal accretion, it is able to accrete a gaseous envelope from the surrounding disc. To model envelope accretion, we have implemented an approximate scheme by calculating analytical fits to the results of the 1D giant planet formation calculations presented in Movshovitz et al. (2010). Because Movshovitz et al. (2010) include the effects of grain growth and settling in their calculations, the opacity in the surface radiative zone of the atmosphere model falls well below the value appropriate to pristine interstellar grains. As a consequence, cores with masses as low as 3 Earth masses are able to accrete massive gaseous envelopes within reasonable protoplanetary disc lifetimes (i.e. 2.7 Myr). We allow gas accretion to occur on to cores once their masses exceed 3 Earth masses in our simulations. The quality of the mass growth fits, compared to the calculations presented by Movshovitz et al. (2010), are demonstrated by fig. 2 in Hellary & Nelson (2012). In units of Earth masses and Myr, this scheme gives a gas accretion rate of

$$\frac{{\rm d}m_{\rm ge}}{{\rm d}t} = \frac{5.5}{9.665} m_{\rm core}^{1.2} \exp\left(\frac{m_{\rm ge}}{5.5}\right). \tag{28}$$

This scheme allows the planet's core to continue to grow due to planetesimal accretion after a gaseous envelope has been acquired, while allowing the rate of envelope accretion to adapt to the varying core mass. This is in agreement with other studies, such as Pollack et al. (1996), that show that the rate of gas envelope accretion increases with the core mass. Furthermore, we note that these models also agree that gas accretion on to a planet transitions from slow settling to runaway accretion at a planet mass between 35 and 40 $\rm M_{\oplus}$. We emphasize this latter point simply because the models that we present later in this paper have difficulty in forming significant numbers of planets that reach this runaway gas accretion mass due to the influence of migration.

Ideally, we would like to incorporate full 1D models of gaseous envelope accretion in our simulations, but at present we have not developed a module for this in our code. While our adoption of fits to the Movshovitz et al. (2010) models allows gas accretion to occur at the rates prescribed in that paper, these fits do not change according to the local conditions in our disc, or according to the time varying planetesimal accretion rate. This is something that we will address in future work.

The gas accretion rate given by equation (28) applies until the planet satisfies the gap formation criterion described above, after which the gas accretion rate switches to the minimum value of that obtained in equation (28) or the viscous supply rate

$$\frac{{\rm d}m_{\rm ge}}{{\rm d}t} = 3\pi\nu\Sigma_{\rm g}, \tag{29}$$

where $\Sigma_{\rm g}$ and ν are the gas surface density and viscosity at the disc location that is 5 planet Hill's radii exterior to the planet's location. This prescription is chosen because the planet sits in a deep gap at this stage of evolution, and so the viscous supply rate of gas must be evaluated at a location in the disc that sits outside of the fully evacuated gap region. We note that our gas accretion routine is mass conservative as gas that is accreted on to the planet is removed from the disc.

2.8 Atmospheric-drag-enhanced capture radius

Although dynamic gas accretion requires the mass of a planet core to exceed 3 $\rm M_{\oplus}$, atmospheres can settle on to planets with significantly lower mass. Although these atmospheres have masses that are dynamically unimportant through their gravitational influence, they can have the important effect of increasing the planetesimal capture radius for the planet through gas drag acting on bodies that have close encounters with the planet. We model this effect by using the prescription described in section 2.5 of Inaba & Ikoma (2003). This model provides an estimate of the atmosphere density as a function of radius, $\rho(R)$. A planetesimal passing through a protoplanet's Hill sphere at a distance $R_{\rm c}$ from the planet will be captured if its physical radius is less than $R_{\rm crit}$ given by the following expression:

$$R_{\rm crit} = \frac{3}{2}\frac{v_{\rm rel}^2 + 2Gm_{\rm p}/R_{\rm c}}{v_{\rm rel}^2 + 2Gm_{\rm p}/R_{\rm H}}\frac{\rho(R_{\rm c})}{\rho_{\rm p}}. \tag{30}$$

Here, $\rho(R_{\rm c})$ is the local density of the protoplanet atmosphere, $\rho_{\rm p}$ is the internal density of the planetesimals, $R_{\rm H}$ is the Hill radius of the protoplanet and $v_{\rm rel}$ is the relative velocity between the two bodies.

The atmosphere model in Inaba & Ikoma (2003) requires calculation of the planet's luminosity. We assume that this is equal to the gravitational energy released by accreted planetesimals

$$L_{\rm p} = \frac{Gm_{\rm p}}{R_{\rm p}}\frac{{\rm d}m_{\rm p}}{{\rm d}t}, \tag{31}$$

where $R_{\rm p}$ is the planet's core radius. The accretion rate of solids on to protoplanets is monitored to determine this accretion luminosity. As this accretion is stochastic in nature, to smooth the accretion rate we calculate and use the average luminosity over temporal windows of 200 local orbits, or 4000 yr, whichever is smaller. Planet luminosities are limited to lie in the range 10^{-9}–10^{-4} $\rm L_{\odot}$.

We limit the effective capture radius of a planet to a maximum of 1/20 of the planet's Hill radius, to avoid overestimating the capture radius for larger planets, as the Inaba & Ikoma (2003) model assumes that the solid core is the main contributor to the gravitating mass. The transition to this limit is also smoothed using the expression

$$R_{\rm capture} = \left[0.5 - 0.5\tanh\left(\frac{m_{\rm p} - 30\,{\rm M}_{\oplus}}{5\,{\rm M}_{\oplus}}\right)\right] R_{\rm atmos} + \left[0.5 + 0.5\tanh\left(\frac{m_{\rm p} - 30\,{\rm M}_{\oplus}}{5\,{\rm M}_{\oplus}}\right)\right] 0.05 R_{\rm H}. \tag{32}$$

Here, $R_{\rm capture}$ is the effective capture radius, $R_{\rm atmos}$ is the atmosphere enhanced capture radius and $R_{\rm H}$ is the Hill radius.

Table 2. Simulation parameters and planet formation modes displayed by the runs: LPG – limited planetary growth, KN – Kamikaze Neptunes, KG – Kamikaze giants and LFS – late forming survivors.

Simulation	Disc mass (MMSN)	Metallicity (solar value)	Planetesimal radius (km)	Formation modes (A/B)
S111A, S111B	1	1	1	LPG/LPG
S1110A, S1110B	1	1	10	LPG/LPG
S121A, S121B	1	2	1	KN/KN
S1210A, S1210B	1	2	10	KN/KN, LFS
S211A, S211B	2	1	1	KN, LFS/KN
S2110A, S2110B	2	1	10	KN/KN
S221A, S221B	2	2	1	KN, KG/KN, KG
S2210A, S2210B	2	2	10	KN/KN
S311A, S311B	3	1	1	KN/KN
S3110A, S3110B	3	1	10	KN/KN, LFS
S321A, S321B	3	2	1	KN, KG/KN, KG
S3210A, S3210B	3	2	10	KN, KG/KN, KG
S411A, S411B	4	1	1	KN/KN
S4110A, S4110B	4	1	10	KN/KN, KG
S421A, S421B	4	2	1	KN, KG/KN, KG
S4210A, S4210B	4	2	10	KN, KG/KN, KG
S511A, S511B	5	1	1	KN, KG/KN, KG
S5110A, S5110B	5	1	10	KN/KN, KG
S521A, S521B	5	2	1	KN, KG, LFS/KN, KG
S5210A, S5210B	5	2	10	KN, KG/KN, KG

2.9 Initial conditions

The simulations were performed using the MERCURY-6 symplectic integrator (Chambers 1999), adapted to include the physics discussed in Section 2. In order to account for the total disc lifetime in all runs, the simulations were run until no protoplanets remained, or for 10 Myr.

All simulations were initiated with 36 planetary embryos, each of mass $0.3\,M_{\oplus}$, separated by 10 mutual Hill's radii, and with semimajor axes lying between 1 and 20 au. These were augmented by thousands of planetesimals, that were distributed in the same semimajor axis interval, with masses equal to $0.03\,M_{\oplus}$ and physical radii equal to either 1 or 10 km (ensuring that they experience appropriate accelerations due to the gas drag forces).

Eccentricities and inclinations for protoplanets and planetesimals were randomized according to a Rayleigh distribution, with scale parameters $e_0 = 0.01$ and $i_0 = 0.^{\circ}25$, respectively. We ignore the effects of turbulent density fluctuations in the disc on the orbital evolution of embedded bodies, as we anticipate that the region of the disc that we simulate will sustain a significant dead zone, with only the innermost $\sim$0.1 au of the disc supporting fully developed turbulence. The initial surface density of solids follows the same profile as the gas, but with an enhancement at and beyond the snow line, similar to the approach used in Hellary & Nelson (2012).

Collisions between protoplanets and other protoplanets or planetesimals were treated as being completely inelastic. A collision results in a single body containing all of the colliding mass. Planetesimal–planetesimal interactions and collisions were not considered in our simulations for reasons of computational speed, and this is one omission from the model that may have a significant influence on the simulation results in regions of high planetesimal density where collisions may become disruptive. The simulations used a minimum time-step of 1 d, corresponding to a minimum semimajor axis of 0.15 au. Bodies with semimajor axes less than this value are removed from the simulation and considered to have impacted on to the central star.

We present simulations for disc masses lying in the range 1–5 times the mass of the minimum mass solar nebula (MMSN; Hayashi 1981), and we also vary the metallicity of the disc so that the initial ratio of solids to gas mass is either 240 or 120 interior to the snow line, the former value being the one expected for the MMSN with a metallicity equal to the solar value. We increase the mass of solids exterior to the snow line smoothly by a factor of 4, as described in Hellary & Nelson (2012). We track the changing compositions of planets during the simulations, as they accrete material that originates either interior or exterior to the snow line.

For each set of physical parameters, we ran two simulations which differed only in the random number seed used to generate the initial particle positions. The full set of simulation parameters are detailed in Table 2.

We set an inner edge to our simulations at 0.15 au. Any body whose semimajor axis becomes smaller than 0.15 au is removed from the simulation.

3 RESULTS

In this section, we begin by discussing the common behaviour associated with the disc evolution and planet migration observed in our simulations. We then present the results of the full *N*-body simulations, where we divide the observed evolution into four distinct modes: *limited planetary growth*; *Kamikaze Neptunes*; *Kamikaze giants*; *late forming survivors*. For each mode, we present the detailed results of one representative run. The modes displayed by each run are listed in Table 2. As the names suggest, the behaviour associated with these different formation modes includes moderate mass growth of planets during the gas disc lifetime, formation of planetary cores that undergo large-scale inward type I migration, formation of giant planets with masses $>30\,M_{\oplus}$ that undergo type II migration into the star (or at least through the inner boundary of the disc model) and formation of super-Earths and Neptune-mass planets late in the disc lifetime that avoid catastrophic migration because of disc dispersal. Not surprisingly, these different

Table 3. Planetary classification parameters based on their composition and the mass fraction of their gaseous envelope. Note that water-rich planets are so-called because they accrete water ice in solid form that originates from beyond the snow line.

Classification	Mass	Rock per cent	Ice per cent	Gas per cent
Rocky terrestrial	$m_p < 3\,M_\oplus$	>95 per cent	<5 per cent	0 per cent
Water-rich terrestrial	$m_p < 3\,M_\oplus$	<95 per cent	>5 per cent	0 per cent
Rocky super-Earth	$3\,M_\oplus \leq m_p < 10\,M_\oplus$	>85 per cent	<5 per cent	<10 per cent
Water-rich super-Earth	$3\,M_\oplus \leq m_p < 10\,M_\oplus$	N/A	>5 per cent	<10 per cent
Mini-Neptune	$3\,M_\oplus \leq m_p < 10\,M_\oplus$	N/A	N/A	>10 per cent
Gas-rich Neptune	$10\,M_\oplus \leq m_p < 30\,M_\oplus$	N/A	N/A	>10 per cent
Gas-poor Neptune	$10\,M_\oplus \leq m_p < 30\,M_\oplus$	N/A	N/A	<10 per cent
Gas-dominated giant	$m_p \geq 30\,M_\oplus$	N/A	N/A	>50 per cent
Core-dominated giant	$m_p \geq 30\,M_\oplus$	N/A	N/A	<50 per cent

formation behaviours correlate with the initial disc mass, metallicity and planetesimal size, and we discuss how these influence the formation and evolution of planetary systems in the simulations. To assist in describing the outcomes of the simulations, we have developed a classification system for the different bodies that are formed, based on their masses and compositions. The classifications and associated parameters used in the definitions are described in Table 3.

3.1 Common behaviour

3.1.1 Gas disc evolution

The viscous and thermal evolution of three disc models are shown in Fig. 1. The top row shows the evolution of the surface density, temperature and H/r profiles for a disc with initial mass equal to 1 × MMSN. The middle and bottom rows show models with initial masses equal to 3 × MMSN and 5 × MMSN, respectively. The times corresponding to each profile displayed in the figure are indicated in the legend contained in the second panel on the top row, expressed as a percentage of the disc total lifetime. These lifetimes are 4.8 Myr for the 1 × MMSN disc, 8 Myr for the 3 × MMSN disc and 9.5 Myr for the 5 × MMSN disc.

Fig. 1 shows that the discs all evolve similarly, with the more massive discs maintaining higher temperatures and H/r values. As the discs evolve viscously, the surface density, temperature and H/r values decrease with time. The decreases in temperature and H/r arise because of the reductions in the viscous heating rates and opacities as Σ decreases. One effect of the decreasing values of H/r with both time and decreasing orbital radius is to allow gap formation to arise for planet masses significantly less than the Jovian mass, and this is one feature that is observed frequently in our N-body simulations: planets of moderate mass (i.e. $m_p \gtrsim 10\,M_\oplus$) migrating inwards at late times and transitioning from type I to type II migration at disc radii <1 au.

The final stages of disc evolution are characterized by the formation of an inner cavity, caused by the inner disc accreting viscously on to the central star while being starved of inflow from further out when the photoevaporative mass-loss exceeds the viscous inflow rate (Clarke, Gendrin & Sotomayor 2001).

3.1.2 Migration behaviour driven by corotation torques

Hellary & Nelson (2012) performed simulations similar to those being presented in this paper, but with simpler power-law disc models, where disc dispersal was modelled through an imposed self-similar exponential decay of the surface density. These models gave rise to a particular expectation for the influence of corotation torques on the migration of low-mass planets, and Hellary & Nelson (2012) explored this behaviour through contour plots that displayed the strength of migration as a function of planet mass and orbital radius. Here, we also consider the expected migration behaviour in our disc models as a function of disc evolution time, planet mass and orbital radius, through the presentation of migration contour plots (or 'migration maps').

We begin by noting that the torque experienced by a low-mass planet embedded in a disc arises because of two components: the Lindblad torque and the corotation torque. The Lindblad torque arises because of spiral density waves that are excited at Lindblad resonances in the disc, and it almost always drives rapid inward migration of planets whose masses exceed an Earth mass. The corotation torque is a non-linear phenomena that is related to the horseshoe orbits followed by fluid elements located in the vicinity of the planet orbital radius. It originates from the entropy and vortensity gradients that exist in protoplanetary discs, and is usually positive, such that it tries to drive outward migration. If the viscous or radiative diffusion time-scales across the horseshoe region are too long, then phase mixing of fluid elements in this region erases these gradients, and the corotation torque saturates (i.e. switches off). Corotation torques are maintained at their maximum values when the viscous/radiative diffusion time-scale is approximately equal to the libration period associated with the horseshoe orbits, and can equal or exceed the Lindblad torque, leading to outward migration. When the viscous/radiative diffusion time-scales are too short, then the corotation torque is reduced considerably in magnitude, and tends towards the value obtained in a linear perturbation analysis. This value is generally too small to counteract the inward migration due to the Lindblad torque.

Considering the torques experienced by a planet with a low initial mass which grows over time, we note that a very low mass protoplanet will have a narrow horseshoe region, x_s, and the libration period associated with the horseshoe orbits will be very long relative to the viscous/radiative time-scales. We therefore expect a low-mass planet to experience a weak corotation torque that is equal to the linear value, and its orbital evolution to be dominated by Lindblad torques. As the planet mass grows, the horseshoe orbit times decrease and eventually equal the viscous and radiative diffusion time-scales. The corotation torque will then be maximized, and the planet may migrate outwards. Further increases in the planet mass cause the horseshoe orbit period to decrease below the viscous

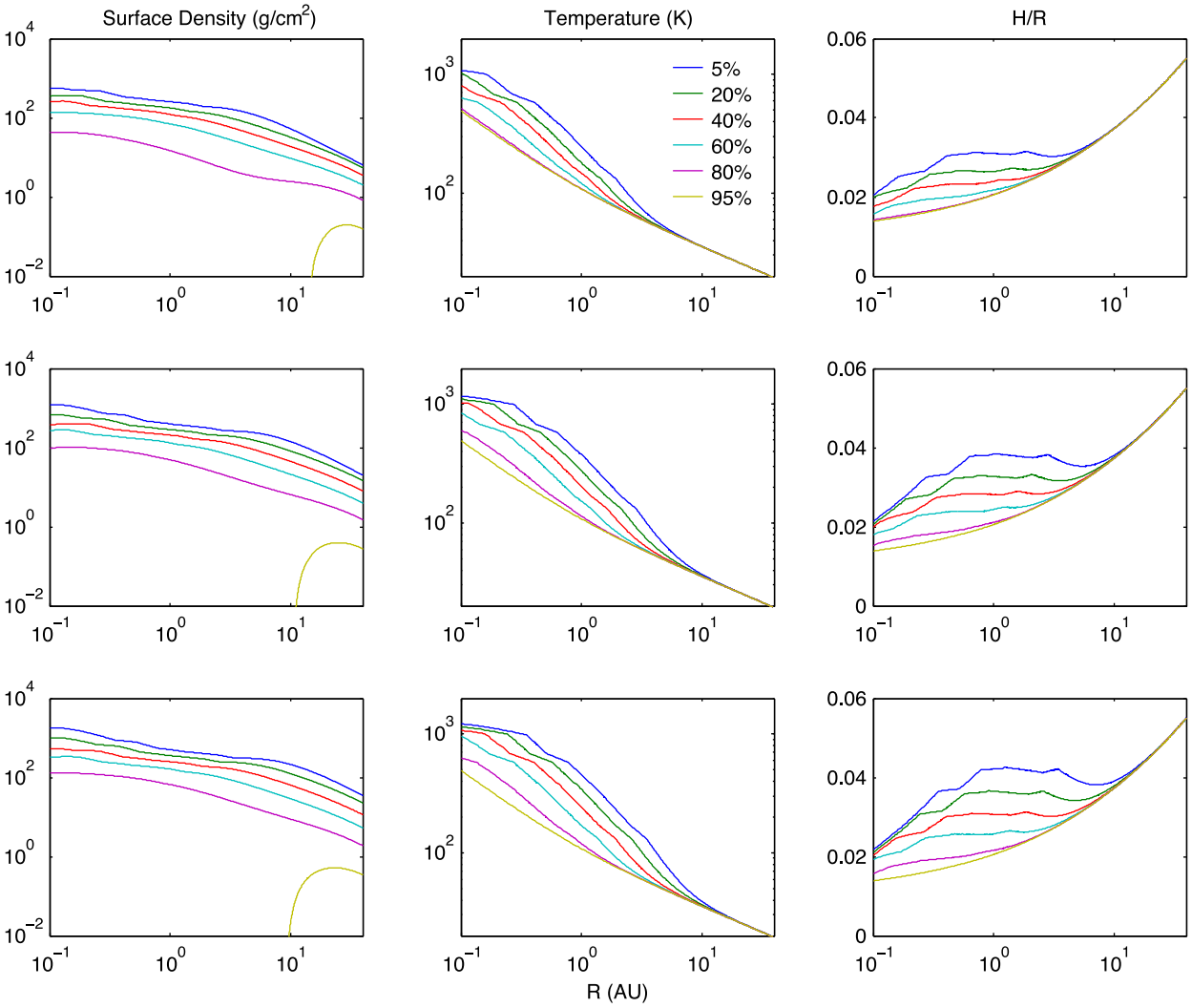

Figure 1. Gas surface densities, temperatures and aspect ratio for 5, 20, 40, 60, 80, 95 per cent (top-bottom lines) of the disc lifetime in 1 × MMSN (top panels, lifetime: 4.8 Myr), 3 × MMSN (middle panels, lifetime: 8 Myr) and 5 × MMSN (bottom panels, lifetime: 9.5 Myr) discs.

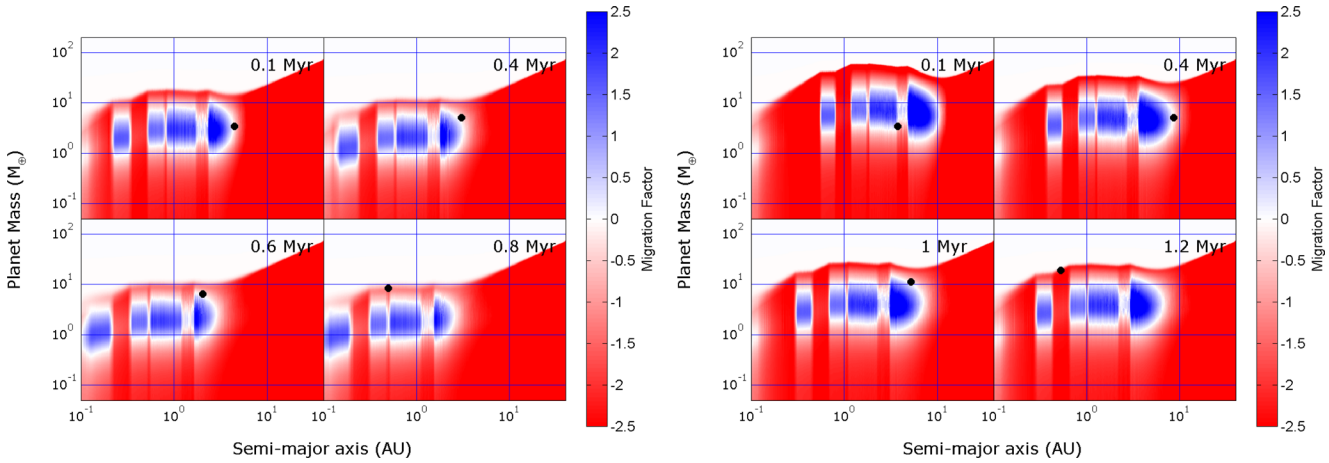

Figure 2. Left-hand panels: contour plots showing regions of outward (blue) and inward (red) migration for a single planet in a 1 × MMSN disc at $t = 0.1$ Myr (top left), $t = 0.4$ Myr (top right), $t = 0.6$ Myr (bottom left) and $t = 0.8$ Myr (bottom right). Right-hand panels: same as left-hand panels but for a 5 × MMSN disc.

and thermal time-scales. A sufficiently massive planet will lose its corotation torque due to saturation, and will migrate inwards rapidly due to the Lindblad torque.

We have performed two separate 'single-planet-in-a-disc' simulations, where a $3\,M_\oplus$ planet is placed in a disc at $a_p = 5$ au with a prescribed mass growth rate, and its orbital evolution, due to the migration torques described in Section 2.5, is followed and shown in Fig. 2. The left-hand panels in Fig. 2 show the migration behaviour for a planet embedded in a disc with mass equal to 1 × MMSN as a function of time. Note that red contours correspond to rapid inward migration due to the dominance of Lindblad torques, and blue contours correspond to strong outward migration. White contours correspond to 'zero-migration zones', where corotation and Lindblad torques balance each other. The structure of the migration contours depend on local disc conditions, and sharp changes in the opacity behaviour can cause sharp transitions in the expected migration behaviour, as shown by the migration maps in Fig. 2. At early times, a planet with mass $\leq 1\,M_\oplus$, located at orbital distances in the range $0.3 \leq r \leq 5$ au, will experience strong inward migration. A planet in the same range of orbital distance with a mass in the interval $1 \leq m_p \leq 10\,M_\oplus$ will experience strong outward migration, and a planet with $m_p > 10\,M_\oplus$ will migrate inwards rapidly.

The location of the planet during the single-planet simulations is denoted by the black dot in Fig. 2.

After 0.1 Myr, we see that it has migrated out to the zero-migration zone located at ∼5 au. As the disc evolves, the migration contours evolve such that the outward migration region moves down in mass and in towards the central star. A planet sitting in a zero-migration zone will move inwards because of the disc evolution, even in the absence of further mass growth. In our single-planet simulation, we see that further mass growth causes the planet to follow the outline of the zero-migration contour, and once its mass approaches $m_p = 10\,M_\oplus$ after 0.8 Myr, it is destined to migrate inwards due to the Lindblad torque.

The right-hand panels in Fig. 2 show a similar scenario, except for a model with disc mass equal to 5 × MMSN. Here, we see that the outward migration contours lie at higher masses and at further distance from the central star, but otherwise show similar behaviour to the 1 × MMSN case. The implications for planet formation arising from this mass dependence is simply that a planetary core which forms at early times may be driven outwards to the zero-migration zone located at $r \sim 10$ au, where in principle it can sit and grow through mutual collisions with additional embryos and planetesimals. This core can grow to a larger mass in the heavier disc prior to saturation of the corotation torque, and may therefore avoid rapid inward migration due to Lindblad torques for a longer period of time. This may not happen in practice, however, because being located in a heavier disc may allow the mass of the planetary core to grow rapidly to a mass at which the corotation torque saturates. Finally, we note that the transition from the red to the white contour at high masses in Fig. 2 corresponds to the planet reaching the local gap forming mass, at which point the planet will undergo type II migration. The contours show that for a more massive disc the transition to gap formation occurs for a higher planet mass, because of the previously mentioned higher temperatures and H/r values.

3.2 Limited planetary growth

In the oligarchic growth scenario, the collisional growth of planets within a disc containing a modest mass in solids is expected to proceed slowly. In the limit of a small enough disc mass, no planets will be able to form with masses that are large enough to accrete gaseous envelopes, even if the spatial density of protoplanets is increased by convergence in zero-migration zones. Planet formation in the lowest mass discs that we have considered, with standard solar metallicities, displays this behaviour, resulting in final systems of planets that are devoid of gaseous envelopes.[2] The simulations labelled as S111A, S111B, S1110A and S1110B displayed this mode of behaviour, and below we describe the results of run S111B in detail.

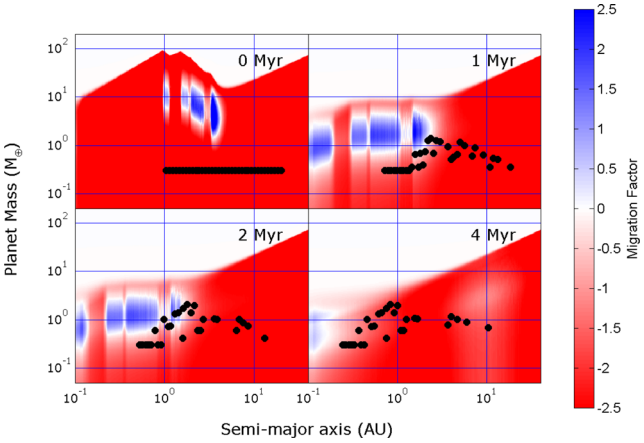

Figure 3. Contour plots showing regions of outward (blue) and inward (red) migration along with all protoplanets for simulation S111B at $t = 0$ yr (top left), $t = 1$ Myr (top right), $t = 2$ Myr (bottom left) and $t = 4$ Myr (bottom right).

3.2.1 *Run S111B*

Run S111B had an initial disc mass equal to 1 × MMSN, solar metallicity and planetesimal radii $R_{pl} = 1$ km. The initial combined mass in protoplanets and planetesimals was equal to $42.5\,M_\oplus$, distributed between disc radii $1 \leq r \leq 20$ au, with the mass in protoplanets being initially equal to $11\,M_\oplus$.

The evolution of the protoplanets in the mass–radius plane is shown in Fig. 3, along with the evolution of the migration torques. The first panel shows that significant planetary growth must occur in order for planets to experience strong corotation torques. The evolution of the protoplanet masses, semimajor axes and eccentricities are shown in Fig. 4. Accretion of planetesimals by protoplanets, and their mutual collisions, quickly leads to the formation of protoplanets with masses $m_p \simeq 1\,M_\oplus$. These bodies experience strong corotation torques, and converge towards the zero-migration zone located at ∼3 au after 1 Myr. The population of planetary cores located initially beyond 10 au grow slowly, and remain in the outer disc throughout the simulation. These are the planets seen to remain at large distance in the middle panel of Fig. 4. The swarm of planets lying interior to this region are drifting in towards the central star slowly because they are being driven largely by the more massive planets that are sitting in the zero-migration zone, and as the gas disc evolves this zero-migration zone drifts

[2] We note that planetary atmospheres may form *via* outgassing, but this effect goes beyond the range of physical processes considered in our models. Furthermore, H-/He-rich envelopes can settle on to relatively low-mass planets (Lammer et al. 2014), and although we consider the effect of this on planetesimal accretion, we do not report gas envelope masses for planets with $m_p < 3\,M_\oplus$.

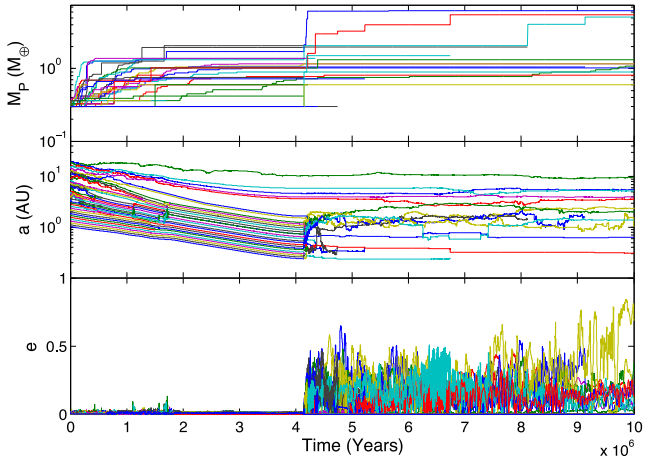

Figure 4. Evolution of masses, semimajor axes and eccentricities of all protoplanets in simulation S111B.

towards the star on a time-scale of ∼4.8 Myr, the gas disc lifetime. In spite of the convergence of protoplanets in the zero-migration zone, Fig. 4 shows that planetary growth leads to the formation of planets with maximum masses $m_{\rm p} \simeq 2\,{\rm M}_{\oplus}$ prior to the gas disc dispersing. Given that our model allows gas accretion to switch on only when the mass of a planet exceeds $3\,{\rm M}_{\oplus}$, this simulation does not result in the formation of any planets that reached the threshold for initiation of gas accretion.

As the gas disc begins to disperse after ∼4 Myr, we see that the planetary eccentricities grow dramatically due to the damping provided by the gas being removed. The planetary orbits begin to cross due to mutual gravitational interactions, and mutual collisions lead to the formation of three super-Earths. The simulation ends at 10 Myr, and at this stage the chaotic orbital evolution and mutual collisions are ongoing such that we have not reached the point of having a final, stable planetary system. At 10 Myr, the three super-Earths have masses 5.5, 6.25 and $5.1\,{\rm M}_{\oplus}$, and orbit with semimajor axes 0.31, 0.64 and 1.39 au, respectively. In addition, there is a collection of lower mass planets with masses in the range $0.7 \leq m_{\rm p} \leq 1.5\,{\rm M}_{\oplus}$ orbiting with semimajor axes between 1.5 and 10 au. All surviving planets are classified as being water rich due to the accretion of material that originated beyond the snow line.

Considering the simulations that we have classed as displaying *limited planetary growth* as a whole (see Table 2), the main difference was observed between runs with 1-km-sized planetesimals and those where planetesimal radii are 10 km. Due to the increased influence of gas drag in damping planetesimal random velocities, and in increasing the effective accretion cross-section of planetary embryos, we find that planet masses are generally larger in the runs with 1 km-sized planetesimals, and correspondingly migration plays a more important role in shaping the resulting planetary systems. Migration plays an important role in determining the overall architecture of all systems that display limited planetary growth, but is sufficiently modest that no planets are lost into the star. The final systems are distributed at large orbital distances compared to some of the highly compact systems that have been discovered in recent years, such as Kepler-11, GJ 581 and HD 69830. In part, this result arises because we initiated the *N*-body simulations with the innermost planetary embryos at 1 au, and a more realistic set-up would have embryos and planetesimals extending down to the sublimation radius at ∼0.1 au. Including this interior population of embryos, however, would only add an additional $\sim 1\,{\rm M}_{\oplus}$ of solid mass to the system, such that its inclusion would not lead to the formation of compact systems of super-Earths containing up to $\sim 30\,{\rm M}_{\oplus}$ of solids as have been observed.

Our somewhat crude approach to modelling the accretion of gaseous atmospheres prevents us from commenting in detail on the mass–radius relation displayed by this population, but we note that the four *limited planetary growth* simulations resulted in the following surviving planets: 47 terrestrials (semimajor axes in the range 0.3–18 au), of which 45 are classified as water rich (the remaining 2 bodies being rocky); 7 water-rich super-Earths (semimajor axes in the range 0.3–1.4 au).

3.3 Kamikaze Neptunes

Increasing the initial mass in planetary embryos and planetesimals in the disc, either by increasing the mass of the disc as a whole, or by increasing the metallicity, should allow more massive planets to grow. At some point, such an enhancement of disc solids will enable the formation of planetary cores with masses $>3\,{\rm M}_{\oplus}$, leading to the accretion of gaseous envelopes. Continued mass growth of these planets will eventually lead to saturation of their corotation torques, as described in Section 3.1, causing rapid inward migration to arise because of Lindblad torques if this phase of evolution occurs in the presence of a substantial gas disc.

It was noted in Section 3.1 that the decrease in H/r at smaller stellocentric distances allows planets of Neptune mass that orbit there to form gaps in the disc. We should then anticipate that the rapid inward migration of intermediate-mass planets into this region will lead to a transition from type I to type II migration. The type II migration time-scale for planets located at 1 au in the disc is $\tau \simeq 1 \times 10^5$ yr, so these planets are likely to migrate into the central star in the absence of a migration stopping mechanism, such as an interior magnetospheric cavity, or unless their inward migration is timed to coincide fortuitously with the final stages of disc dispersal through photoevaporation.

In this section, we describe the results of simulations in which super-Earth and Neptune-mass planets form relatively early in the disc lifetime, so that photoevaporation of the disc cannot halt their migration. These planets migrate through the whole system of embryos and planetesimals, and through the inner edge of our computational domain. This mode of evolution was observed in 18 of the 40 runs performed, as listed in Table 2.

3.3.1 Run S211A

Simulation S211A has an initial disc mass equal to 2 × MMSN, solar metallicity, planetesimal radii equal to 1 km and an approximate gas disc lifetime of 6.7 Myr. The total initial mass in solids is equal to $84\,{\rm M}_{\oplus}$.

The full time evolution of the planet semimajor axes, eccentricities and masses are shown in Fig. 5. Snapshots showing the mass, orbital radii and migration behaviour of planets at key points during the evolution are shown in Fig. 6. During the first 0.5 Myr, planets with semimajor axes <2 au migrate inwards slowly without accreting many planetesimals or experiencing mutual collisions, so their masses remain $<0.5\,{\rm M}_{\oplus}$ during this time. Protoplanets with semimajor axes >2 au accrete planetesimals and undergo mutual collisions, with three planets accreting enough mass to initiate gas accretion. The most rapidly growing of these reaches mass $m_{\rm p} = 10\,{\rm M}_{\oplus}$ after 0.5 Myr, while orbiting at 5 au.

Over the next 0.25 Myr, the $10\,{\rm M}_{\oplus}$ planet continues to accrete gas and planetesimals, while migrating outwards towards the

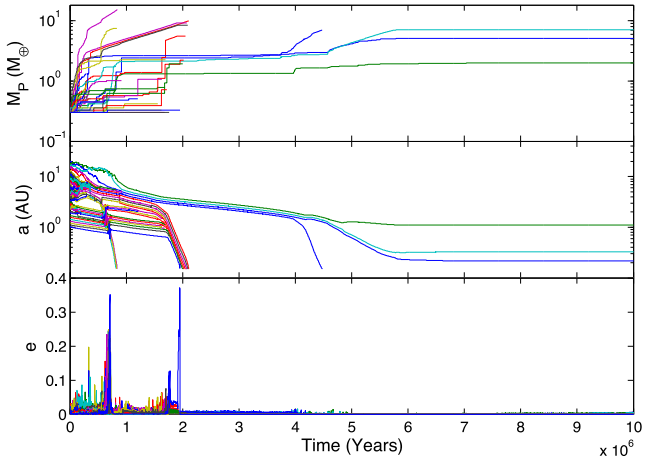

Figure 5. Evolution of masses, semimajor axes and eccentricities of all protoplanets in simulation S211A.

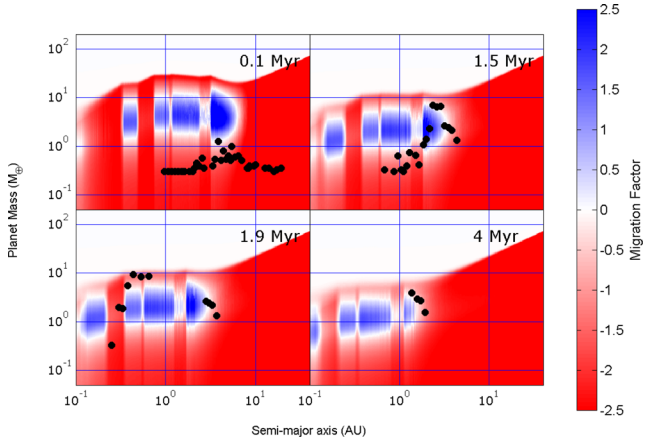

Figure 6. Contour plots showing regions of outward (blue) and inward (red) migration along with all protoplanets for simulation S211A at $t = 0.1$ Myr (top left), $t = 1.5$ Myr (top right), $t = 1.9$ Myr (bottom left) and $t = 4$ Myr (bottom right).

zero-migration zone located at ∼6 au. It grows massive enough for the corotation torque to saturate, leading to a period of rapid inward migration. At 0.78 Myr, the now-Neptune-mass planet opens a gap when it reaches semimajor axis 0.5 au, and transitions to type II migration. After a further 5×10^4 yr, this planet migrates through the inner boundary of the computational domain, taking two lower mass planets with it that are trapped in an interior resonant chain. During the large-scale inward migration, a large group of low-mass planets is scattered to larger radii, instead of migrating in resonance with the migrating group, due to mutual gravitational interactions that cause them to leave the mean motion resonances and scatter off the Neptune-mass planet. This is a similar scenario, albeit with a lower mass primary migrator, to that of Jupiter-mass planets scattering terrestrial planets while migrating inwards as described in Fogg & Nelson (2009).

Planetary accretion and migration continues among the exterior population of embryos during the migration and loss of the Neptune-mass planet. Looking at the top and middle panels of Fig. 5, we can see that three planets continue to grow slowly through planetesimal and gas accretion between 0.3 and 1.6 Myr. These planets drift inwards slowly because they sit in a zero-migration zone that moves towards the central star as the disc evolves, as shown in the top-right panel of Fig. 6. When the planets reach masses ∼8 $M_\oplus$, the corotation torques saturate, and these planets migrate inwards rapidly, catching a resonant chain of seven planets. The three most massive planets form gaps in the disc after 1.9 Myr when they reach semimajor axes ∼0.5 au, before they all migrate past the inner boundary at 2.1 Myr. Low-mass planets within the resonant chain either collided with the more massive planets, or were swept through the inner boundary. The most massive planet to pass through the inner boundary in this chain was 10 $M_\oplus$, with a gaseous envelope that contained 68 per cent of its total mass.

After 2.1 Myr, four planets remain in a resonant chain, orbiting at a few au, with masses $<3\,M_\oplus$. Slow inward migration continued for the next 2 Myr, at which point the innermost planet accreted a large number of planetesimals from a cluster that it encountered, increasing its mass above 3 $M_\oplus$ and initiating gas accretion. 4 Myr after the start of the simulation, the corotation torque for this planet saturates, and it undergoes faster inward migration, before opening a gap at 0.5 au and type II migrating through the inner boundary at 4.5 Myr with a mass of 7 $M_\oplus$. The three remaining planets continue to drift in slowly due to the inward drift of the zero-migration zone, and for two of these three planets gas accretion was initiated after they accreted planetesimals so that their masses exceeded 3 $M_\oplus$. These planets underwent a period of more rapid migration, but because this last phase of evolution occurred as the gas disc was being dispersed, they accreted only limited amounts of gas and halted their migration without passing through the inner boundary. The final configuration of the system consisted of three surviving planets orbiting with semimajor axes 0.22, 0.33 and 1.1 au, with masses 5.1, 7.2 and 2 $M_\oplus$. The innermost two planets have gas envelope fractions of 13 and 53 per cent, respectively, meaning they are classified as mini-Neptunes. The final low-mass terrestrial planet is classified as water rich owing to its initial location beyond the snow line.

A total of 18 other simulations showed similar evolution histories to that just described. These had disc masses varying between 1 and 5× MMSN. In each simulation, sub-Neptune and Neptune-mass planets migrated inwards rapidly through type I migration, after saturation of their corotation torques, before entering a phase of type II migration when at orbital radii equal to a few tenths of an au. During the large-scale migration, terrestrial-mass planets were scattered to larger radii, and some were forced to migrate inwards in resonant chains. Surviving planets in these systems had a maximum mass of 7.2 $M_\oplus$ (from the run S211A described above), and the majority had masses between 1 and 5 $M_\oplus$.

It is worth noting that an individual run can display more than one mode of planet formation defined by our classification system. According to our nomenclature, run S211A displays the formation modes dubbed as *Kamikaze Neptunes* and *late forming survivors*.

3.4 Kamikaze giants

For a disc with a significant mass in solids, either because it has a large overall mass or because the disc has an enhanced metallicity, we might expect massive cores to form that are capable of accreting significant gaseous envelopes, leading to the formation of *giant planets* with masses $m_p \geq 30\,M_\oplus$ (as per our definition of a giant planet given in Table 2). As discussed in Section 3.1, having a larger gas disc mass leads to higher temperatures and H/r values, and this pushes the zero-migration zones to larger radii and allows corotation torque saturation to occur only for higher mass planets, as demonstrated by Figs 1 and 2. Higher mass planets are also likely to transition to slower type II migration at larger radii, and this

combination of factors favours the growth of more massive planets by allowing them to remain in the disc for longer periods of time.

The following simulation provides a specific example of giant planets being able to form in more massive discs through the combination of the effects just discussed. As discussed later in Section 5, the survival against migration of an isolated 30 $M_\oplus$ giant planet, which forms through gas accretion on to a 15 $M_\oplus$ core, can only occur if the planet opens a gap and starts type II migrating inwards from an orbital radius $\gtrsim$6 au. The formation and survival of a Jovian-mass planet requires gap opening and the initiation of type II migration at orbital radii $\gtrsim$20 au. This sequence of events is not observed to occur in any of our simulations, such that all giant planets formed during the runs are lost via migration into the central star.

3.4.1 *Run S421A*

Run S421A has an initial disc mass equal to 4 × MMSN, and has twice the solar metallicity. Planetesimal radii are 1 km, and the approximate gas disc lifetime equals 8.8 Myr. The total mass of solids is equal to 337 $M_\oplus$, providing a substantial feedstock that enhances the likelihood of forming massive planetary cores.

The first 0.5 Myr of the evolution of planet's semimajor axes, masses and eccentricities are shown in Fig. 7, and the full time evolution is shown in Fig. 8. A mass–radius plot of the planets and their migration behaviour at specific moments during the evolution are shown in Fig. 9. Close inspection of the top two panels of Fig. 7 shows that during the first 0.15 Myr, numerous embryos grow in mass, largely through the accretion of planetesimals, and start to accrete gas as their masses exceed 3 $M_\oplus$. These planets experience strong, unsaturated corotation torques, and migrate out towards their zero-migration zones that are located at between 4 and 8 au. Continued mass growth above ∼30 $M_\oplus$ for the outermost of these planets leads to saturation of the corotation torque, and a period of rapid inward migration. As this dominant planet migrates inwards, it captures the two other massive planets in mean motion resonance, one of which tries to migrate outwards because it experiences a strong, positive corotation torque from the disc, but is forced to move in with the dominant migrator because of the resonance. Some of the interior lower mass protoplanets are also captured into the resonant chain, whereas other bodies escape long-term resonant capture, and are scattered outwards through interaction with the

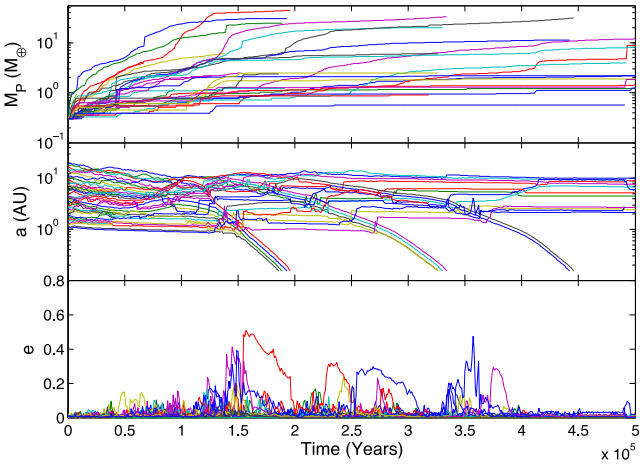

Figure 7. Evolution of masses, semimajor axes and eccentricities of all protoplanets for the initial 500 000 yr in simulation S421A.

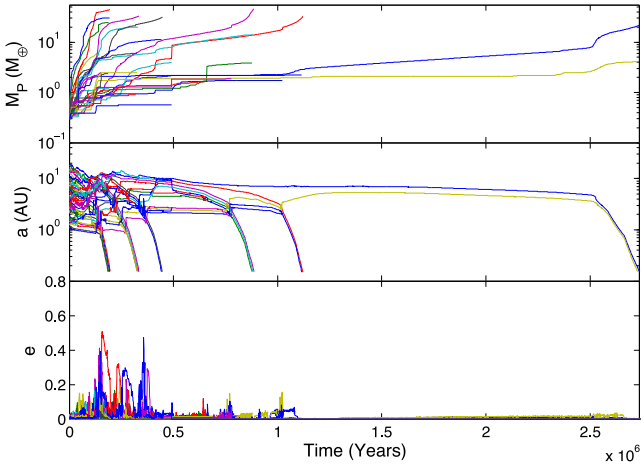

Figure 8. Evolution of masses, semimajor axes and eccentricities of all protoplanets in simulation S421A.

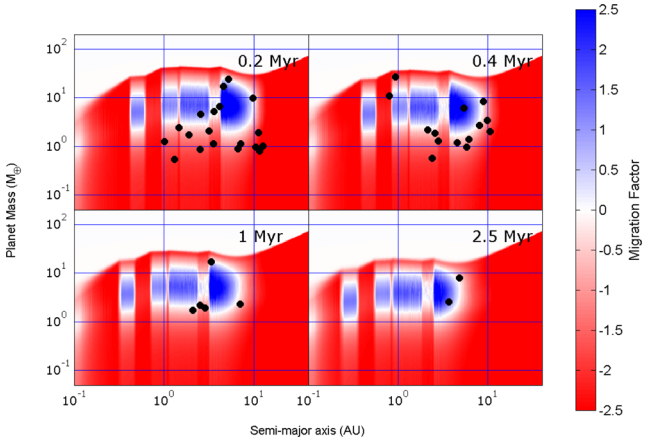

Figure 9. Contour plots showing regions of outward (blue) and inward (red) migration along with all protoplanets for simulation S421A at $t = 0.2$ Myr (top left), $t = 0.4$ Myr (top right), $t = 1$ Myr (bottom left) and $t = 2.5$ Myr (bottom right).

three most massive planets. These scattering events lead to the bursts of eccentricity observed in the bottom panels of Figs 7 and 8. The three massive planets start to form gaps in the disc when they reach semimajor axes ∼0.8 au, and at this point their gas accretion rate is limited by the rate that gas can be supplied viscously, and their migration transitions from type I to type II. The planets then type II migrate into the central star on a time-scale of 5 × 10^4 yr, with masses 45, 30 and 25 $M_\oplus$. We classify the first two of these planets as *core-dominated giants*, because their early formation in the presence of a massive disc of solids leads to >85 per cent of their mass being in solids. The least massive planet of the three is classed as a *gas-poor Neptune*.

During the next 0.3 Myr, two massive, gas-accreting planets form, causing two more periods of rapid inward migration that involve giant planets with masses 33 and 31 $M_\oplus$, respectively. As with the initial large-scale migration episode described above, some small protoplanets were forced to migrate in resonance with the more massive planets, whilst other protoplanets were scattered outwards. As these planets accreted planetesimals at a slower rate, due to the planetesimal depletion caused by the earlier generation of planet formation and migration, the ratio of gas to solids in these planets was higher. As a result, the two core-dominated giants accreted

gaseous envelopes that accounted for 30 and 37 per cent of the total mass, respectively. After 0.5 Myr has elapsed, 33 per cent of the original protoplanets remain in the simulation.

Throughout the remainder of the simulation, three more massive planets form and undergo rapid inward type I migration before opening gaps at semimajor axes between 0.5 and 0.8 au, and undergoing type II migration through the inner boundary at times 0.9, 1.1 and 2.7 Myr, respectively, as illustrated by Fig. 8. The masses of these planets at this point are 47, 32 and 22 $M_\oplus$, with gas envelopes containing 71, 67 and 53 per cent of the total mass, respectively. The two most massive of these planets are therefore classified as *gas-dominated giants*, and the third planet is classified as a *gas-rich Neptune*. In comparing gas envelope percentages of late forming giant planets with those that formed earlier, it is observed that early forming giants are very heavy-element rich with modest H/He envelopes, while late forming giants are more abundant in H/He because of the depletion of planetesimals and embryos by the earlier generations of planet formation and migration.

After the final rapid migration event, no protoplanets remained in the simulation, resulting in the end of the run before the disc had fully dispersed.

The general behaviour described above for run S421A is exhibited by a number of the runs whose evolution is classified as *Kamikaze giants*, although some of the runs do retain a population of remnant low-mass planets at the end, and some *late forming survivors*. Two runs that produced giant planets with significantly larger masses were S511A and S511B. In each of these runs, collisions involving already massive bodies, orbiting at between 2 and 2.5 au, resulted in the formation of a planet with a mass that was greater than the runaway gas accretion mass. Each of these planets opened gaps in the disc and type II migrated inwards, reaching final masses of $\sim$90 $M_\oplus$ before migrating through the inner boundary of the disc. Simulations that formed giant planets, but which did not produce collisions involving already massive bodies, generally formed giant planets with masses in the range $30 \leq m_p \leq 45\,M_\oplus$. This is because rapid inward type I migration led these planets to open gaps in the disc at small orbital radii $\leq$1 au before runaway gas accretion could occur, leaving minimal time to accrete gas while undergoing the final stages of type II migration. From a total of 18 simulations with comparable results, 57 giant planets were formed and migrated through the inner boundary, with a range of masses between 30 and 92 $M_\oplus$.

3.5 Late forming survivors

As has been shown in Sections 3.3 and 3.4, early forming Neptunes and giant planets are unable to survive in the disc if they form when the remaining disc lifetimes exceed the migration timescales. If planets grow slowly, and survive early generations of giant planet formation and avoid large-scale inward migration in resonant convoys, and begin accreting gas during the latter stages of the disc lifetime, then planets with significant gaseous envelopes can survive.

In the following subsection, we discuss one specific example of a simulation where the late formation and survival of gaseous planets occur after earlier generations of Neptune-mass and giant planets have migrated through the system.

3.5.1 Run S521A

Simulation S521A had an initial disc mass equal to 5 $\times$ MMSN, twice the solar metallicity, 1-km-sized planetesimals and an approximate disc lifetime of 9.5 Myr. The total mass of solids was equal to 421 $M_\oplus$.

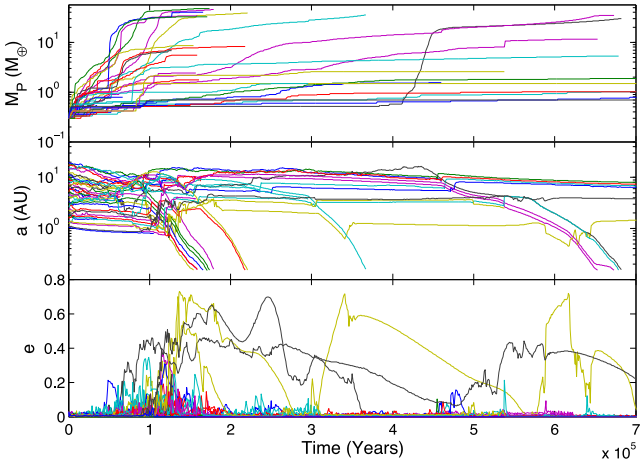

Figure 10. Evolution of masses, semimajor axes and eccentricities of all protoplanets for the initial 700 000 yr in simulation S521A.

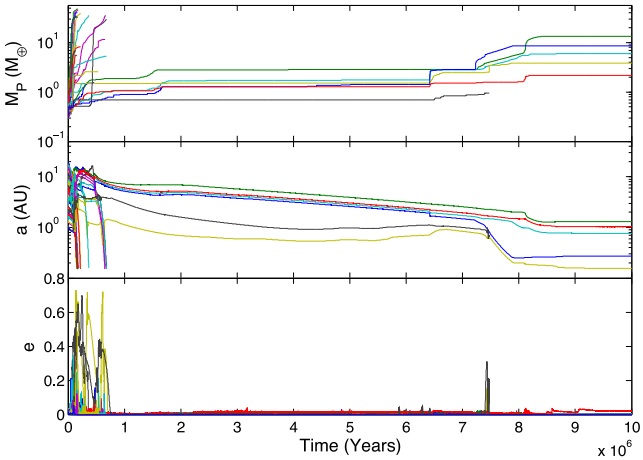

Figure 11. Evolution of masses, semimajor axes and eccentricities of all protoplanets in simulation S521A.

The initial 0.7 Myr of evolution of the semimajor axes, eccentricities and masses are shown in Fig. 10, and the total time evolution is shown in Fig. 11. Migration maps are shown for the epochs 0.1, 0.3, 0.5 and 5 Myr in Fig. 12, with black dots denoting protoplanet positions in the mass–radius plane. As shown in Fig. 10, five massive planets form with masses between 12 and 42 $M_\oplus$ during the first 0.1 Myr. Rapid growth of solid cores and gas accretion cause the corotation torques for these bodies to saturate, and they undergo inward type I migration. Gap formation ensues for all these planets as they migrate interior to 1 au, and between the times 0.12–0.18 Myr they migrate through the inner boundary with final masses between 32 and 47 $M_\oplus$. These planets had gas envelope fractions between 8 and 13 per cent, so are all classed as *core-dominated giants*. After a further 5×10^4 yr, another core-dominated giant migrates through the inner boundary with a mass $m_p = 39\,M_\oplus$, and an envelope fraction of 16 per cent. The large-scale migration of these giant planets caused three low-mass planets to migrate through the inner boundary, and inspection of Fig. 10 shows that numerous interior

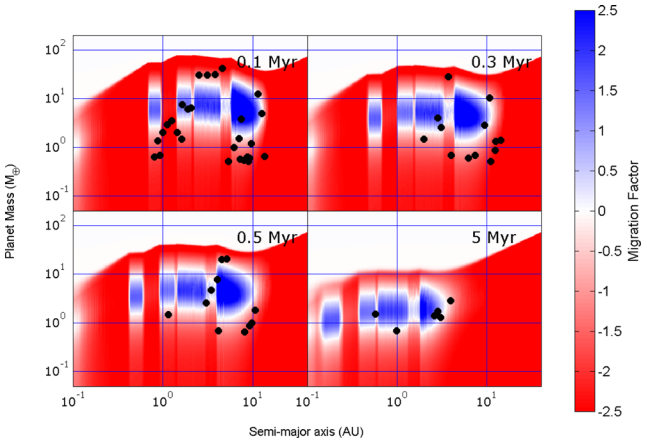

Figure 12. Contour plots showing regions of outward (blue) and inward (red) migration along with all protoplanets for simulation S521A at $t = 0.1$ Myr (top left), $t = 0.3$ Myr (top right), $t = 0.5$ Myr (bottom left) and $t = 5$ Myr (bottom right).

planets were scattered to larger orbital radii during this period of evolution.

Over the next 0.5 Myr, three additional giant planets accrete gas, before migrating through the inner boundary at times 0.36, 0.67 and 0.68 Myr, respectively. These giant planets leave the simulation with masses $m_p = 36$, 34 and 30 $M_\oplus$, with gas envelope fractions 34, 54 and 35 per cent, respectively. Two low-mass planets resonantly migrate with the latter two giant planets, while six other low-mass planets are scattered to larger radii. Fig. 12 shows three of these migration events occurring, along with a snapshot of the system after 5 Myr showing the six remaining low-mass planets. These six planets then drift inwards while sitting in zero-migration zones for the next 6 Myr, while accreting planetesimals at a slow rate, and without accreting gas from the disc due to their masses being $<3\,M_\oplus$.

After 7.2 Myr, two planets accrete a swarm of planetesimals, allowing them to begin gas accretion. These planets then proceed to migrate inwards while accreting gas, and forming gaps within the disc, until the combined action of photoevaporation and viscous evolution begins to remove the inner disc after 7.9 Myr, leaving the planets stranded at small orbital radii. Complete disc dispersal occurs after 9.5 Myr, leaving a total of five planets: a 13 $M_\oplus$ gas-rich Neptune with an 8 $M_\oplus$ solid core and a 5 $M_\oplus$ envelope orbiting at 1.3 au (not too different from interior models for Neptune and Uranus; Podolak, Podolak & Marley 2000), an 8.6 $M_\oplus$ mini-Neptune with gas envelope mass fraction equal to 41 per cent orbiting at 0.27 au, and a 6 $M_\oplus$ mini-Neptune orbiting at 0.77 au with gas envelope mass fraction equal to 31 per cent. The two remaining planets were a 3.8 $M_\oplus$ water-rich super-Earth orbiting at 0.16 au and a 2 $M_\oplus$ water-rich terrestrial planet with semimajor axis $\sim$1 au.

The late formation of these super-Earths/mini-Neptunes and gas-rich Neptune allowed them to survive migration into the star, while simultaneously limiting the amount of mass available to be accreted due to the earlier generations of planets that were lost from the system.

In Section 5, we examine the conditions under which gas accreting planets can survive type II migration within the disc models that we present here, and the maximum masses that they can reach through gas accretion prior to removal of the disc by photoevaporation.

3.6 Summary of all runs

A suite of 40 simulations has been performed, with disc masses between 1 and 5 $\times$ MMSN, metallicity being either solar or two times solar, and planetesimal radii being either 1 or 10 km. For each permutation of this parameter set, we ran two realizations by changing the random number seed used to set the initial particle positions and velocities. The final outcomes of all simulations, after 10 Myr of evolution, are shown in Fig. 13.

We now comment on how the different initial conditions in the simulations influenced their final outcomes by discussing briefly each of the panels in Fig. 13. We remind the reader that the labelling convention for the simulations is such that a run labelled S$N_1N_2N_3$ has disc mass $N_1 \times$ MMSN, metallicity enhancement factor N_2 and planetesimal radii N_3 km, where N_3 is either 1 or 10. Each panel contains both the set A simulation results (blue symbols) and those from set B (red symbols).

3.6.1 S111 and S1110

These models have the lowest disc masses and metallicites. The growth of planets occurred relatively slowly in all four runs, and the low mass of the gaseous disc resulted in only modest migration. No material was lost through the inner boundary of the computational domain in these runs. Systems of planets were formed consisting of more massive super-Earths orbiting with semimajor axes in the range $0.3 \leq a_p \leq 1.4$ au, and less massive terrestrials orbiting at larger semimajor axes $0.3 \leq a_p \leq 18$ au. The planetary systems continue to evolve through mutual interactions and collisions up to and beyond the end of the simulations.

3.6.2 S121 and S1210

These models initially have twice the mass in solids compared to the previous set. We see that doubling the mass in solids has the tendency of increasing the mass growth of planets, particularly those that are orbiting at greater distances from the central star. Planets were lost from the system by migrating into the central star in both of these run sets. We see that run S1210B results in a 9 $M_\oplus$ planet orbiting at $a_p \simeq 0.2$ au, and all runs result in systems of terrestrial and super-Earths orbiting between $0.6 \leq a_p \leq 12$ au.

3.6.3 S211 and S2110

These models have double the disc mass in both solids and gas compared to runs S111 and S1110. We see that this enhances both the growth in mass of the final planets, and also increases the degree to which they have migrated. We note that these simulations result in substantial loss of solid material on to the central star through the formation and migration of super-Earth and Neptune-mass planets early during the disc lifetime.

3.6.4 S221 and S2210

Doubling the metallicity leads to a dramatic change in the results compared to runs S211 and S2110. We see that out of the four runs in the sets S221 and S2210, only S221B and S2210A resulted in any surviving planets, and these are each $\sim$1 $M_\oplus$ bodies orbiting at $a_p \sim 1$ au. Planetary mass growth in these runs in the presence of a substantial gas disc results in almost all planets migrating into the central star.

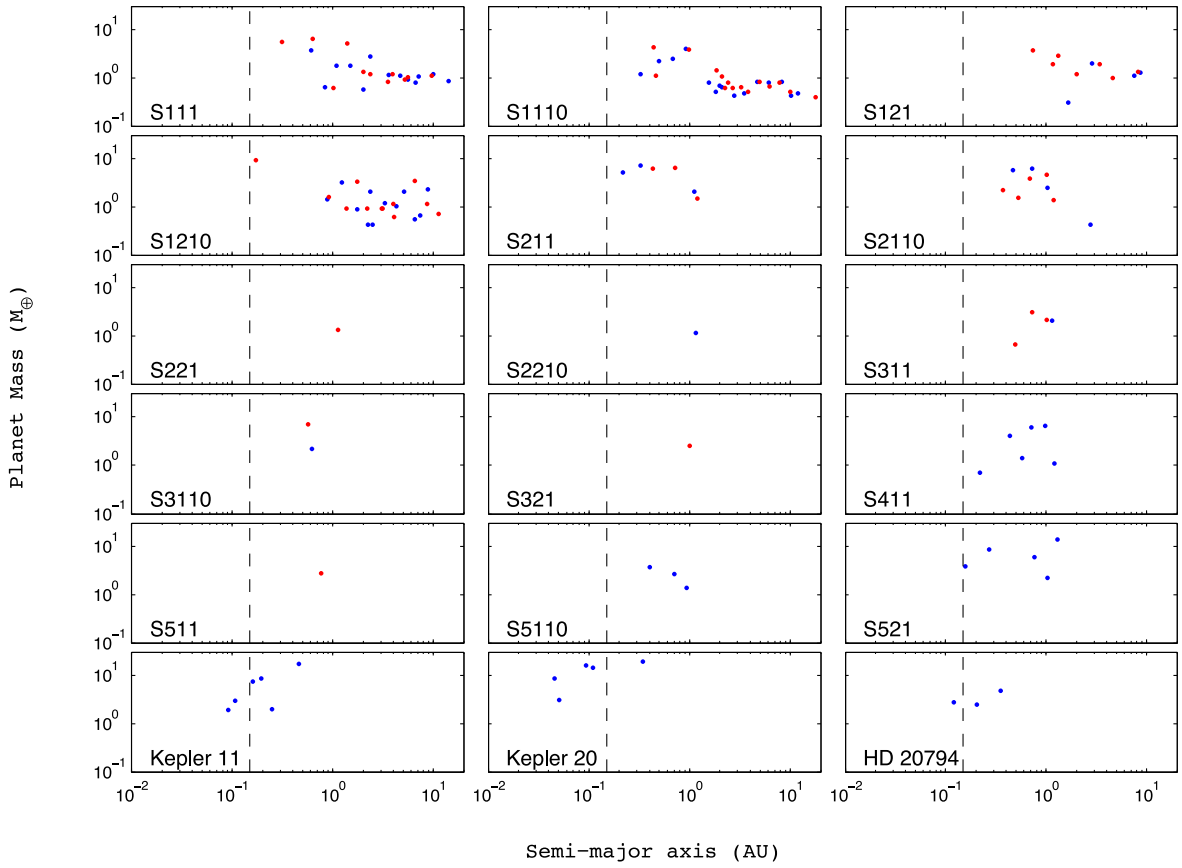

Figure 13. Final masses versus semimajor axes for all planets formed in all simulations. The blue symbols represent the set A simulations, and red symbols represent set B. The inner edge of the computational domain is shown by the vertical dashed line in each panel. For comparison, a selection of observed systems are also shown. Simulations that resulted in all planets migrating through the inner edge of the computational domain are not shown.

3.6.5 S311, S3110, S321 and S3210

These runs continue the trend of almost all solid mass being evacuated from the disc through the formation of rapidly migrating giant planets ($m_p > 30\,M_\oplus$), or Neptunes and super-Earths, in the presence of a substantial gas disc.

3.6.6 S411, S4110, S421 and S4210

Of these runs, only S411A resulted in any planets surviving to the end of the simulations. S411A is an example of a run in which there is sufficient disc mass to allow multiple generations of planets to grow and migrate into the star, while leaving sufficient mass remaining in the disc near the end of the gas disc lifetime to allow a collection of terrestrial planets and super-Earths to form and survive.

3.6.7 S511, S5110, S521 and S5210

These runs follow the now familiar pattern of early formation of super-Earths, Neptunes and giant planets, resulting in them migrating into the central star. In all but run S521A, almost all of the solid mass is lost from the system prior to dispersal of the gas disc. S521A is another example of a simulation that resulted in late forming surviving planets, resulting in a system of two mini-Neptunes, a gas-rich Neptune, a water-rich super-Earth and a water-rich terrestrial, with masses between $2 \leq m_p \leq 13\,M_\oplus$ and semimajor axes $a_p \leq 1.3$ au.

Considering the simulations collectively, we note that the final outcomes mirror the three essentially different modes of behaviour that were described in Sections 3.2, 3.3, 3.4 and 3.5: (i) moderate growth and migration, resulting in closely packed systems of low-mass super-Earths and terrestrials, but no Neptunes or giant planets; (ii) growth of super-Earths, Neptunes and giant planets early in the gas disc lifetime, resulting in catastrophic migration into the central star of all, or almost all, of the initial mass in solids; (iii) late formation of terrestrials, super-Earths and Neptunes from the material left over after previous generations of planet formation and catastrophic migration in high-mass discs.

Across all simulations, 57 giant planets were formed, with none surviving migration. The largest planet formed was $92\,M_\oplus$ (two such planets formed in our simulation suite), but due to its formation early in the disc lifetime it migrated through the inner boundary. Several Neptune-mass planets also followed this course of growth and migration, generally doing so in lower mass discs.

4 COMPARISON WITH OBSERVATIONS

Although our simulation set does not constitute a population synthesis model, because we have not used a Monte Carlo approach to selecting initial conditions from a distribution of possibilities based on observational constraints, it is interesting nonetheless to compare our results with the observational data, so that we can see where model improvements are required. Fig. 14 is a mass versus period diagram for the surviving planets from the

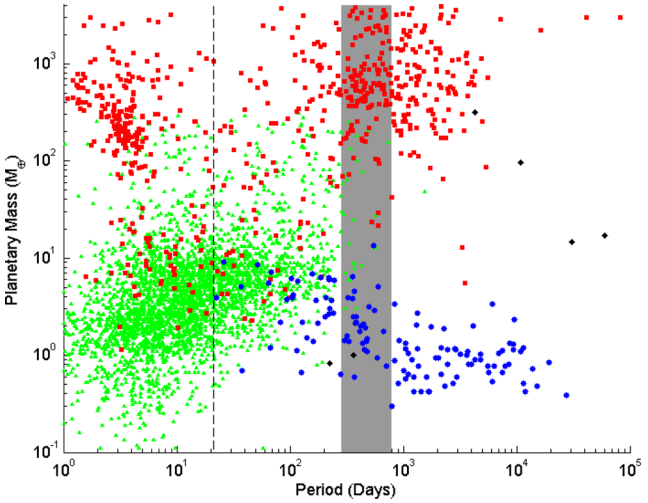

Figure 14. Mass versus period plot, comparing observed exoplanets (red squares) and *Kepler* candidates (green triangles) with our simulation results (blue circles) and the Solar system (black diamonds). The dashed line indicates the 0.15 au cutoff point in our simulations, whilst the grey zone indicates the habitable zone (Kasting, Whitmire & Reynolds 1993).

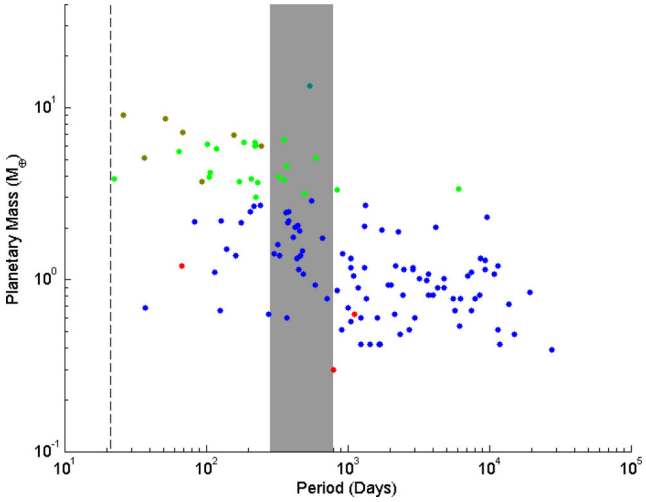

Figure 15. Mass versus period plot for the simulation results where symbol colour indicates planet classification. (Red: rocky terrestrial. Blue: water-rich terrestrial. Green: mini-Neptune. Brown: water-rich super-Earth. Cyan: gas-rich Neptune). The dashed line and grey zone are identical to that in Fig. 14.

simulations, along with all confirmed exoplanets and *Kepler* candidates (sourced from www.exoplanets.eu, Schneider et al. 2011). The vertical dashed line located at ∼20 d shows the position of the inner edge of our computational domain, so our simulation results cannot be compared with observed exoplanets with orbital periods less than this value.

The shorter period terrestrial-mass planets, super-Earths and Neptune-like planets from the simulations lie in the parameter space occupied by the confirmed exoplanets and *Kepler* candidates. The longer period terrestrial-mass planets and super-Earths from the simulations, however, lie in an area that is sparsely populated by observed exoplanets because of observational biases in the radial velocity and transit techniques. These planets are best observed by the microlensing technique, but so far the yield from microlensing surveys is insufficient to provide strong constraints on models. In future, the *PLATO* mission (Rauer et al. 2013) will provide information on this population of low-mass exoplanets on orbits with intermediate periods.

A clear failing in the simulation results is the lack of surviving giant planets at any orbital period. We explore this issue in greater depth in Section 5 below, but the primary reason for this is that planets in our simulations rarely undergo runaway gas accretion because inward type I migration transports intermediate-mass planets to small orbital radii, where gap formation and type II migration follow. The type II migration time-scale for planets orbiting at orbital radii <1 au is short, leading to the planets quickly migrating through the inner boundary of the simulation domain.

Fig. 15 shows a mass versus period diagram for the surviving planets from the simulations, where the planets are colour coded according to the classification scheme described in Table 3. There is an abundance of water-rich terrestrials at all semimajor axes due to large-scale migration from beyond the ice line bringing volatile-rich material into the inner regions. For planets with masses $>3\,M_\oplus$, mini-Neptunes are the dominant population, where planets have >10 per cent of their mass in gas. Gas-poor super-Earths typically formed at small semimajor axes, closer to the central star than the habitable zone. The largest surviving planet formed in the simulations is a gas-rich Neptune located in the habitable zone, as discussed in Section 3.5.

5 CONDITIONS FOR GIANT PLANET FORMATION AND SURVIVAL

As has been shown in Sections 3 and 4, although our simulations managed to form giant planets with substantial gaseous envelopes, none of them managed to survive against migration into the star. We did not include the effects of an inner disc cavity in this work, which would stop migration and the loss of these giants, but inclusion of such a cavity would lead to a model prediction that essentially all stars have close-orbiting planets, contradicting the observational data. Furthermore, a central cavity cannot explain the longer period giant planet systems that are observed to exist in abundance, as illustrated by Fig. 14.

We now investigate the conditions required for a giant planet to form and survive within the context of our model. We present two suites of calculations below. The first adopts the standard model for gas accretion used in the simulations presented in previous sections. The second uses a model for accretion that is calibrated against a 2D hydrodynamic simulation of an accreting and migrating planet that is embedded in a gaseous disc, following a similar approach to the runs presented in Nelson et al. (2000).

5.1 Standard accretion prescription

We ran a suite of single-planet simulations where a $15\,M_\oplus$ planetary core is embedded at various locations (1, 2, 3, ..., 20 au) in discs with masses that range between 0.2 and 0.8 × MMSN, in an attempt to find out what final planet masses and orbital radii are achieved. The initial conditions are such that we allow the $15\,M_\oplus$ core to accrete gas as described in Section 2.7. This prescription uses analytical fits to the Movshovitz et al. (2010) gas envelope accretion calculations, and when the planet reaches the gap opening mass gas accretion changes to the rate at which gas can be supplied viscously $\dot{m} = 3\pi\nu\Sigma$, where this quantity is calculated in the disc at a distance from the planet equal to $r - r_\mathrm{p} = 5R_\mathrm{H}$. Type II

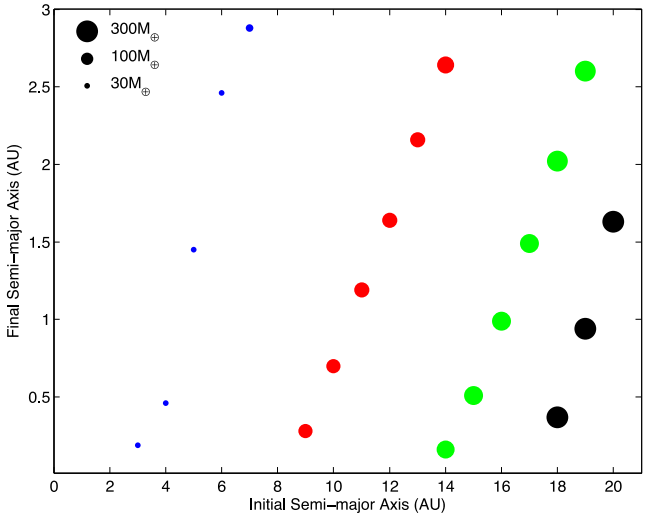

Figure 16. Final versus initial semimajor axes of planets in discs undergoing standard photoevaporation that start with masses: 0.2 × MMSN (blue), 0.4 × MMSN (red), 0.6 × MMSN (green) and 0.8MMSN (black).

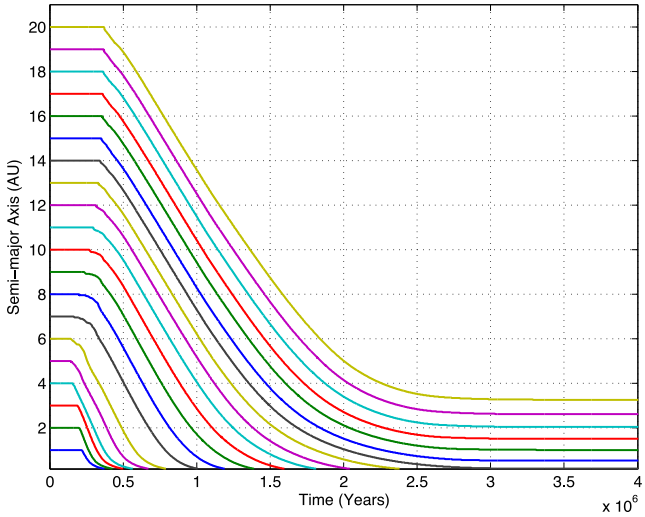

Figure 17. Semimajor axis evolution of 15 $M_\oplus$ gas accreting cores in discs with initial masses of 0.6 × MMSN.

migration is switched on when the gap opening mass is reached. Type I migration is neglected for these simulations so that the effects of type II migration can be analysed. To examine the potential effects of increasing the photoevaporation rate of the disc, we adapt the standard photoevaporation routine to account for an enhanced rate of dispersal when the disc interior to the planet's orbit has been cleared due to tidal truncation by the planet, allowing ionizing photons to illuminate the inner edge of the disc directly. The direct photoevaporation prescription that we adopt is taken from Alexander & Armitage (2007) and Alexander & Armitage (2009), where the photoevaporative mass-loss rate is given by

$$\frac{\mathrm{d}\Sigma_{\mathrm{direct}}}{\mathrm{d}t} = 2C_2\mu m_{\mathrm{H}} c_{\mathrm{s}} \left(\frac{f_{41}}{4\pi\alpha_{\mathrm{B}} h R_{\mathrm{in}}^3}\right)^{1/2} \left(\frac{R}{R_{\mathrm{in}}}\right)^{-2.42}. \quad (33)$$

Here, $C_2 = 0.235$, α_{B} is the Case B recombination coefficient for atomic hydrogen at 10^4 K, having a value of $\alpha_{\mathrm{B}} = 2.6 \times 10^{-19}\,\mathrm{m^3\,s^{-1}}$ (Cox 2000), and r_{in} is the radial location of the inner disc edge.

For the standard photoevaporation routine, we observe that in simulations starting with disc masses equal to 0.2 × MMSN, the starting semimajor axis for a 15 $M_\oplus$ core that accretes gas, reaches the gap opening mass, and survives type II migration is 3 au, indicating that any planet that forms and opens a gap interior to 3 au will migrate into the star. Planets forming exterior to this radius will survive migration due to disc dispersal, and their final masses and stopping locations will depend on their initial formation semimajor axes. For higher mass discs, the formation zone that guarantees survival lies at increasing distance from the star, with the survival radii for 0.4, 0.6 and 0.8 × MMSN disc being 9, 14 and 18 au, respectively. The masses of these survivors are 126, 224 and 298 $M_\oplus$, respectively. Fig. 16 shows the starting and final semimajor axes, and the final planet masses, for all survivors as a function of disc mass and starting position. The final planet mass increases as the initial semimajor axis increases, as expected, since the planet has an increased local disc mass throughout its migration, along with an increased time to accrete. Fig. 17 shows the evolution of the semimajor axes for the full set of 0.6 × MMSN simulations. Migration slows as planets reach the inner regions of the disc, where the amount of remaining disc mass determines if survival is possible.

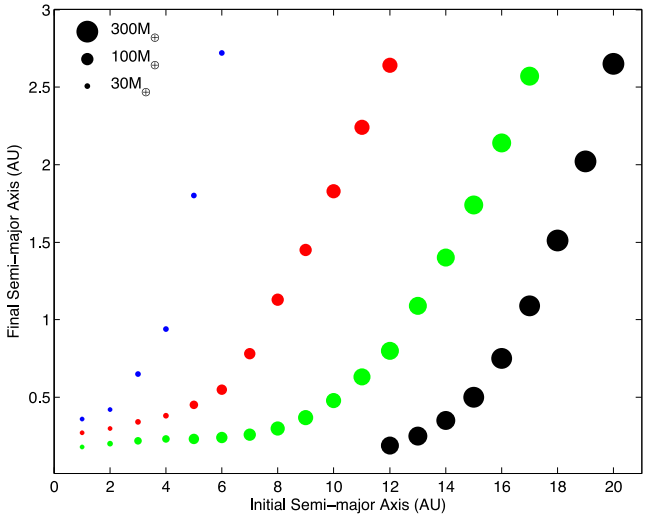

Figure 18. Final versus initial semimajor axes of planets in discs undergoing direct photoevaporation, with initial disc masses being: 0.2 × MMSN (blue), 0.4 × MMSN (red), 0.6 × MMSN (green) and 0.8 × MMSN (black).

Planets forming exterior to 14 au were found to survive, where the disc lifetime for this model is 2.9 Myr.

Results for the simulations that adopt the direct photoevaporation routine described above are shown in Fig. 18. Planets forming between 1 and 20 au in discs with 0.2, 0.4 and 0.6 × MMSN discs all survive migration. The formation of a gap by a planet allows the inner disc to accrete on to the star within the time taken for the planet to migrate all the way to the inner boundary of the simulation domain. Consequently, as the planet migrates inwards, the inner disc disappears, allowing rapid photoevaporation of the exterior disc through direct illumination. This planet-induced disc removal is rapid enough to ensure survival for all planets that form in the models described above. Simulations with disc mass 0.8 × MMSN result in planets migrating into the star unless they form with semimajor axes $\geq$12 au.

Planets with large initial semimajor axes in both sets of simulations behaved similarly, especially for larger disc masses. In both sets of simulations, a Jupiter-mass planet formed by gas accretion

on to the 15 $M_\oplus$ core only if the core started accreting gas beyond 20 au, and the initial disc mass was at least 0.8 times MMSN. This shows that Jupiters *can* form in our simulations, but only if the core starts to accrete gas at large distance from the central star, giving it sufficient time to accrete a massive gaseous envelope prior to halting its migration due to disc dispersal. Higher mass discs will allow Jovian-mass planets to form and survive, but as the disc mass increases, migration into the central star becomes more likely, so the initial formation radius must increase correspondingly.

In summary, in order for our standard model to form surviving Jupiters, it is necessary for planetary cores to accrete gas and open gaps at large radii. They must do this at a sufficiently late epoch, so that viscous evolution and photoevaporation have depleted the disc sufficiently that it will disperse before the planet migrates into the star. For the particular parameters adopted in our models, Jovian-mass planets must initiate their formation through gas accretion on to solid cores out beyond 20 au. As described in previous sections, in almost all of our simulations in which a gas accreting core forms, it migrates inwards to $r_\mathrm{p} \simeq 0.8$ au before forming a gap and type II migrating into the star, preventing a massive gas giant planet from forming. In none of the simulations does a core form at, or experience disc-driven migration out to, the distance required for a gas giant planet to form and survive against type II migration. Furthermore, we do not observe any planet–planet scattering that results in planetary cores being flung out to these outer disc regions.

5.2 Alternative gas accretion prescription

In order to examine how well our results for gas accretion and migration agree with hydrodynamic models of planets embedded in discs, we have performed three 2D simulations of migrating and accreting planets embedded in gaseous discs. In our fiducial hydrodynamic simulation, the parameters adopted were $\alpha = 2 \times 10^{-3}$, $H/r = 0.05$ and initial planet mass $m_\mathrm{p} = 50\,M_\oplus$. The surface density profile $\Sigma(r) = \Sigma_0 r^{-1/2}$, and the disc mass was normalized so that the characteristic mass within the planet orbit $\pi r_\mathrm{p}^2 \Sigma(r_\mathrm{p}) = 264\,M_\oplus$. The inner and outer boundaries of the computational domain were located at $0.1 r_\mathrm{p}$ and $2.5 r_\mathrm{p}$, respectively, where r_p denotes the initial orbital radius of the planet, here assumed to be $r_\mathrm{p} = 5$ au. The second simulation adopted identical parameters, except that $H/r = 0.0245$. The third simulation was the same as the first, except the initial disc mass was increased by a factor of 3. The simulations were performed using the NIRVANA code (Ziegler & Yorke 1997; Nelson et al. 2000), with resolution $N_r = 800$ and $N_\phi = 400$, and adopted the accretion routine described in Kley (1999) that removes gas from within the planet Hill sphere on the dynamical time-scale. Our choice of initial planet mass $m_\mathrm{p} = 50\,M_\oplus$ means that the planet should be in the runaway gas accretion regime from the beginning of the simulation (Pollack et al. 1996; Movshovitz et al. 2010).

In general, there is good agreement between the numerous hydrodynamic simulations that have been published concerning the gas accretion rate on to a giant planet (Bryden et al. 1999; Kley 1999; Lubow, Seibert & Artymowicz 1999; Nelson et al. 2000; Bate et al. 2003; D'Angelo, Kley & Henning 2003; Gressel et al. 2013). It should be noted that these simulations do not resolve the gas flow all the way on to the surface of the planet, in general, and normally adopt a simple equation of state, and so essentially assume that gas accretion on to the planet itself occurs at the same rate that the surrounding protoplanetary disc supplies gas to the planet Hill sphere. In order to reach the planet, this gas must lose its angular momentum, and at the present time it is not known what mechanism is responsible for this angular momentum exchange, or how quickly it operates (Szulágyi et al. 2014). Putting these complications to one side, we simply note that our fiducial hydrodynamic simulation predicts that the planet accretes essentially all of the gas in its feeding zone (defined to be $m_\mathrm{iso} = 2\pi r_\mathrm{p} \Sigma_\mathrm{g}(r_\mathrm{p}) \Delta r$, where we set $\Delta r = 4\sqrt{3} R_\mathrm{H}$) during the gap formation process, and once this 'gas isolation mass', m_iso, has been reached, the planet continues to accrete at close to the viscous supply rate through the gap while undergoing type II migration. The second hydrodynamic simulation with $h = 0.0245$ was designed to test what happens when the planet is very close to, or equal to, the gap forming mass when it starts to undergo runaway gas accretion. In this case, we find that only a fraction of the gas in the feeding zone is accreted because the planet efficiently opens a gap as it starts to accrete. The third simulation was designed to examine what happens when the planet is too low in mass to open a gap when it first enters the runaway gas accretion phase, but the feeding zone contains significantly more mass than is necessary for the planet to reach the local gap formation mass. In this case, we find that the planet is able to efficiently accrete a large fraction of the mass in the feeding zone before transitioning to accretion at the viscous supply rate, because gas accretion occurs more rapidly than gap formation in this case.

Given the results of these hydrodynamic simulations, we have implemented a new model of gas accretion into our *N*-body plus 1D disc code that matches the results of the hydrodynamic calculations. For a planet that reaches the runaway gas accretion phase prior to reaching the gap forming mass, we apply the following steps:

(i) Noting that a partial gap is formed even by a planet that is below the formal gap opening mass, we calculate the surface density fraction that is available for accretion as given by Crida & Morbidelli (2007)

$$F_\Sigma(P_\Sigma) = \begin{cases} \frac{P_\Sigma - 0.541}{4} & \text{if } P_\Sigma < 2.4646 \\ 1 - \exp\left(\frac{P_\Sigma^{3/4}}{-3}\right) & \text{if } P_\Sigma \geq 2.4646 \end{cases}, \tag{34}$$

where

$$P_\Sigma = \frac{3H}{4 r_\mathrm{p} \sqrt[3]{q/3}} + \frac{50\nu}{q r_\mathrm{p}^2 \Omega_\mathrm{p}}. \tag{35}$$

(ii) Calculate the gas isolation mass, m_iso, given above using $\Sigma_g = \Sigma_g F_\Sigma$.

(iii) Allow the planet to grow rapidly to m_iso by removing gas from the disc around the planet and adding it to the planet. Once the planet reaches this mass, it transitions to type II migration and accretes at the viscous supply rate.

When implementing the above prescription, we define the moment when runaway accretion occurs as being when $\frac{\mathrm{d}m}{\mathrm{d}t} \geq 2\,M_\oplus$ per 1000 yr. We note that a planet that does not reach the runaway gas accretion mass prior to reaching the local gap forming mass will instead transition directly to gas accretion at the viscous supply rate, and will undergo type II migration, without accreting the mass in its feeding zone. The gap formation criterion used in the calculations presented in this section is $3H/(4R_\mathrm{H}) + 50\nu/(q r_\mathrm{p}^2 \Omega_\mathrm{p}) < 1$. In Fig. 19, we plot the semimajor axis versus time, the mass versus time, and the mass versus semimajor axis for the fiducial 2D hydrodynamic simulation, and a set of 1D single-planet-in-a-disc runs where the viscous supply rate of gas is calculated at different locations in the disc that lie at different distances from the planet. Also plotted in this figure are the results obtained using the standard gas accretion routine used in the full *N*-body simulations presented earlier in this paper. Close inspection of this figure shows that the

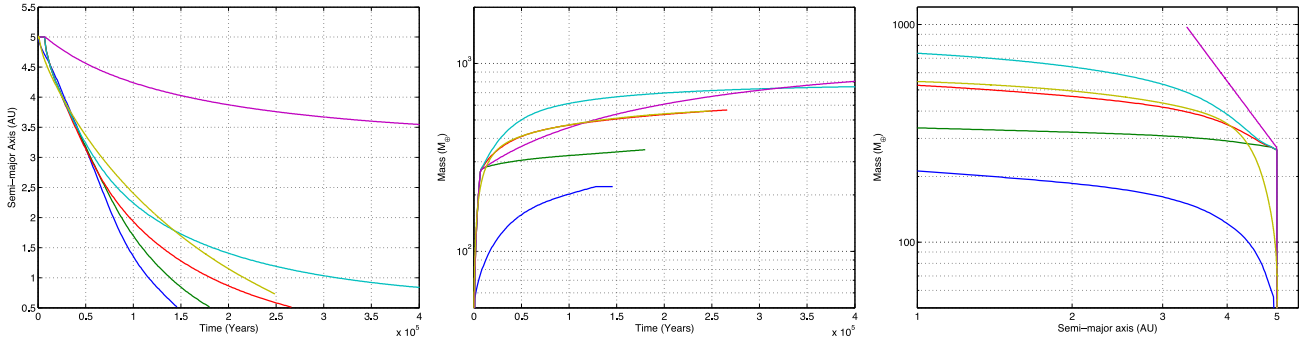

Figure 19. Left-hand panel: semimajor axis versus time. Middle panel: mass versus time. Right-hand panel: mass versus semimajor axes. Each panel shows results for 50 $M_\oplus$ gas accreting cores in a 1 × MMSN disc with different accretion routines: standard accretion prescription (blue), alternative accretion prescription evaluated at distances 5, 10, 15 R_H from the planet (green, red, cyan), results from 2D hydro simulation (yellow) and results from the Mordasini et al. prescription (purple).

new accretion routine is a dramatic improvement over our standard gas accretion prescription, with best agreement between 1D models and the 2D hydrodynamic simulation occurring when the viscous supply rate is calculated at 10 Hill radii exterior to the planet in the 1D simulations. The standard accretion routine adopted for the *N*-body simulations presented earlier predicts too low an accretion rate compared to the 2D hydrodynamic simulations, but it should be noted that this makes essentially no difference to the results of the full *N*-body simulations, as only 2 out of 40 runs resulted in a planet undergoing runaway gas accretion at an orbital radius >0.8 au. Those simulations simply did not produce planets with properties that would allow the new accretion routine to significantly change the outcome of the simulations.

One issue of particular interest is why our *N*-body simulations produce no surviving giant planets, whereas the population synthesis models of Mordasini et al. (2009), for example, are successful in forming large numbers of surviving gas giants. We have implemented the migration and gas accretion prescriptions for gap opening planets from Mordasini et al. (2009), and the results are shown by the purple curves in Fig. 19. We note that the gradient of the curve shown in the mass versus semimajor axis plot equals $-\pi$, in agreement with Mordasini et al. (2009). It is clear that there is strong disagreement between the results obtained using the Mordasini et al. prescriptions and our hydrodynamic simulation and best fitting 1D model. The problem lies in their inclusion of the factor $2\Sigma_g r_p^2/m_p$ in the migration torque when migration enters the so-called planet-dominated regime with $m_p > 2\Sigma_g r_p^2$, as this factor causes the migration to slow down too much while gas accretion continues to occur at the viscous supply rate. We note that we set up our fiducial hydrodynamic simulation with $2\Sigma_g r_p^2 = 168\,M_\oplus$, so that migration quickly enters the planet-dominated regime when the planet reaches the Jovian mass, which it does once reaching an orbital radius $r_p \sim 4$ au. Towards the end of the simulation, the planet mass reaches 550 $M_\oplus$ while at an orbital radius $a_p \sim 1$ au such that the above migration slowing factor predicts that the migration speed will reduce by a factor of ∼30. The hydrodynamic simulation does not reproduce this strong slowing of migration. The gradient observed in the mass versus semimajor axis plot for the hydrodynamic run approaches the value −0.1 rather than $-\pi$, because of the faster migration. This result suggests that the population synthesis calculations over estimate the number of gas giant planets that are able to form and survive in the models.

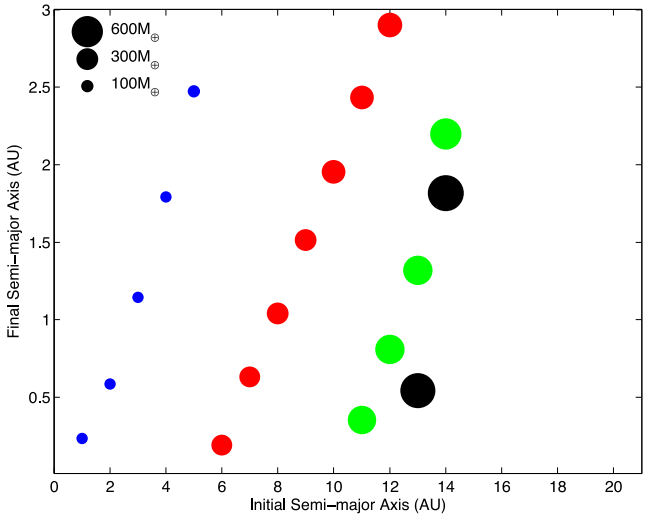

Figure 20. Final against initial semimajor axes of planets in discs undergoing rapid accretion and no direct photoevaporation, starting with specific masses: 0.2 × MMSN (blue), 0.4 × MMSN (red), 0.6 × MMSN (green) and 0.8MMSN (black).

We have re-run the 1D single-planet simulations presented in Section 5.1 to examine how the predictions of giant planet survival change with the new gas accretion prescription, and the results are shown in Figs 20 and 21 for the standard and direct photoevaporation prescriptions, respectively. We see that the conditions required for the survival of gas giants are now quite different from those obtained using the standard accretion routine, and suggest that surviving giant planets can form closer to the star. Nonetheless, we also see that giant planets must still start to undergo runaway gas accretion at orbital radii $r_p \gtrsim 10$ au in order for massive gas giant planets to survive. As such, this shows that inclusion of the new gas accretion prescription will not change the results of our simulations dramatically, because of the fact that type I migration of planetary cores to orbital radii $r_p \sim 0.8$ au almost always occurs prior to runaway gas accretion switching on. It therefore remains a significant challenge for our simulations to form cores that undergo runaway gas accretion at large enough radii that they can survive as giant planets, even when a more efficient gas accretion prescription is adopted.

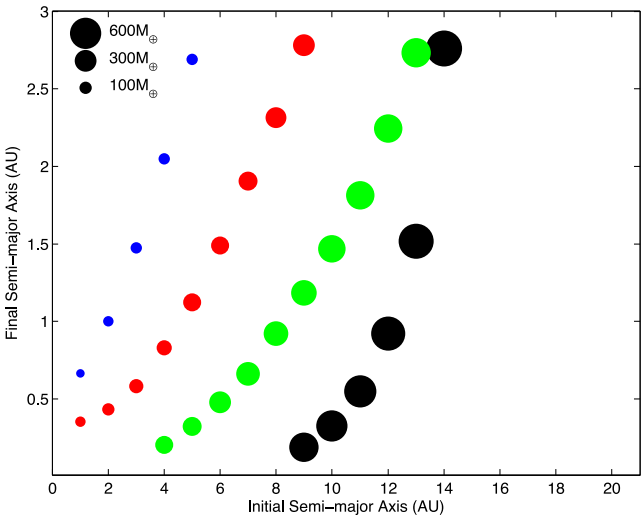

Figure 21. Plot of final semimajor axis versus initial semimajor axis of planets in discs undergoing rapid accretion and direct photoevaporation, starting with disc masses 0.2 × MMSN (blue), 0.4 × MMSN (red), 0.6 × MMSN (green) and 0.8 × MMSN (black).

6 DISCUSSION AND CONCLUSIONS

We have presented the results of *N*-body simulations of planet formation in thermally evolving viscous disc models. The main results to come out of this study may be summarized as follows.

(i) Planetary growth in low-mass discs (i.e. $\sim$1 × MMSN) occurs relatively slowly, leading to the formation of closely packed systems of terrestrial-mass and super-Earth planets that orbit with semimajor axes in the range $0.3 \leq a_{\rm p} \leq 20$ au. The close-packed nature of these systems means that they continue to evolve over time-scales that are longer than the 10 Myr run times of our simulations. We anticipate that these systems will achieve final stable architectures after a period of collisional accretion lasting $\gtrsim$100 Myr.

(ii) Increases in the masses of solids available for planet building, either by increasing the solids-to-gas ratio in a disc or by increasing the total disc mass (solids and gas), lead to multiple generations of Neptune-mass ($\sim$15 $\mathrm{M}_{\oplus}$) and giant planets ($\gtrsim$30 $\mathrm{M}_{\oplus}$) forming and migrating into the star. This arises because the growth of planets to masses $m_{\rm p} \gtrsim 10\,\mathrm{M}_{\oplus}$ causes corotation torques to saturate, allowing rapid inward type I migration to occur. Once planets reach the inner disc regions where $H/r \sim 0.02$, these planets may form gaps and type II migrate into the central star. This process of formation and catastrophic migration of planets occurred in the majority of our simulations, resulting in either only low- and intermediate-mass planets surviving, or in extreme cases no planets surviving at all.

(iii) In a few cases, a final generation of super-Earths and Neptune-mass planets forms and migrates while the gas disc is undergoing its final stage of dispersal, allowing these final planets to survive.

(iv) The most massive planet to form in our simulations had $m_{\rm p} = 92\,\mathrm{M}_{\oplus}$, but was lost from the system due to type II migration. This planet formed through a collision between two already massive planets, leading to the formation of a body that was able to undergo runaway gas accretion while orbiting at $\sim$2.3 au. 2 out of 40 simulations displayed this behaviour. More typically, giant planets in our simulations achieved final masses in the range $30 \leq m_{\rm p} \leq 45\,\mathrm{M}_{\oplus}$ before migrating into the star. The most massive surviving planet from all simulations was a gas-rich Neptune with $m_{\rm p} = 13\,\mathrm{M}_{\oplus}$.

(v) We have examined in detail the conditions required for gas giant planets to form and survive within the context of our model. We find that a planet must accrete gas, form a gap and initiate inward type II migration at an orbital radius $\gtrsim$20 au in order to form a surviving Jovian-mass planet. In our simulations, essentially all planets migrate into the inner disc regions, and reach the local gap forming mass prior to undergoing runaway gas accretion, explaining why our runs never form Jovian-mass planets.

(vi) Comparing 2D hydrodynamic simulations of accreting and migrating planets with single-planet calculations performed using the *N*-body code coupled to the 1D disc model yields interesting results. First, this comparison has allowed us to develop a more accurate mass accretion prescription for planets that enter the runaway gas accretion phase prior to reaching the local gap forming mass. When applying this prescription to the question of when Jovian-mass planets can form and survive, we find that a planet must initiate runaway gas accretion at an orbital radius $\gtrsim$10 au. Secondly, we find that planets migrate inwards at a rate that is substantially faster than that has been assumed in some population synthesis models (e.g. Mordasini et al. 2009), particularly when in the so-called planet-dominated regime, explaining why these statistical models are more successful at forming giant planets that survive migration and grow to large masses than the models presented here. We suggest that the type II migration prescription being used in these population synthesis models causes planet migration to slow down too much, while allowing planets to accrete at the viscous rate. This suggests that the population synthesis models overpredict the numbers of gas giant planets that form and survive.

The conclusions that we have drawn about the formation and survival of gas giant planets imply that Jovian-mass exoplanets, and the gas giants in our Solar system initiated formation much further out in the disc than their currently observed locations. Our current understanding of disc-driven migration makes it difficult to understand how this can happen for an isolated planet, as the 20–30 $\mathrm{M}_{\oplus}$ precursors to gas giant planets migrate inwards rapidly. If this conclusion is taken at face value, then one possible explanation for formation at large radius is that some cores are gravitationally scattered out to large radii through dynamical interactions between massive cores closer to the star, and these cores accrete gas as they type II migrate back into the inner disc regions. We note, however, that this mode of behaviour has not been observed in any of the simulations. A previously suggested explanation for the fact that the giant planets in our Solar system did not migrate over large distances is that Jupiter and Saturn entered into 3:2 mean motion resonance with each other, with Uranus and Neptune entering mean motion resonance with Saturn and each other (Masset & Snellgrove 2001; Morbidelli et al. 2007). This configuration can cause the sum of the migration torques to cancel, preventing migration of all the planets. This scenario, however, cannot be used to explain how the giant planets managed to form in the first place, as the cancellation of torques only operates once massive gap forming planets have formed. The most likely explanation of why our models fail to form surviving gas giant planets is that our current knowledge of planet migration and/or basic disc physics remains incomplete, and that some key ingredient is missing from the models that we have presented.

In future work, we will consider a broader range of disc models etc. to examine whether or not there exists a reasonable range of physical parameters that allows the oligarchic growth picture of

planet formation, combined with our best current understanding of migration and disc evolution, to generate systems of planets that match the types of planetary systems that are being discovered by observations. We will also include refinements to the current model, such as extending the inner boundary to smaller radii so that the simulations have the possibility of forming planets with sub-20 d periods, and incorporating a self-consistent gas envelope accretion model that responds to the changing disc conditions (Papaloizou & Terquem 1999; Papaloizou & Nelson 2005) and planetesimal accretion rates. It is only by refining the physics of the model, and by extending the range of initial conditions, that we can construct a fair test of whether or not the basic planet formation scenario that we have presented can successfully reproduce the observed systems. The evidence presented in this paper suggests that achieving this goal will be difficult in disc models with smooth, self-similar radial structures that allow large-scale migration of planets to proceed unimpeded.

ACKNOWLEDGEMENTS

GALC acknowledges the support of an STFC PhD studentship. The simulations presented in this paper were performed on the QMUL HPC facility purchased under the SRIF initiatives.

REFERENCES

Adachi I., Hayashi C., Nakazawa K., 1976, Prog. Theor. Phys., 56, 1756
Alexander R. D., Armitage P. J., 2007, MNRAS, 375, 500
Alexander R. D., Armitage P. J., 2009, ApJ, 704, 989
Alibert Y., Carron F., Fortier A., Pfyffer S., Benz W., Mordasini C., Swoboda D., 2013, A&A, 558, A109
Batalha N. M. et al., 2011, ApJ, 729, 27
Bate M. R., Lubow S. H., Ogilvie G. I., Miller K. A., 2003, MNRAS, 341, 213
Bell K. R., Lin D. N. C., 1994, ApJ, 427, 987
Bell K. R., Cassen P. M., Klahr H. H., Henning T., 1997, ApJ, 486, 372
Bitsch B., Kley W., 2010, A&A, 523, A30
Boss A. P., 1997, Science, 276, 1836
Bryden G., Chen X., Lin D. N. C., Nelson R. P., Papaloizou J. C. B., 1999, ApJ, 514, 344
Chambers J. E., 1999, MNRAS, 304, 793
Clarke C. J., Gendrin A., Sotomayor M., 2001, MNRAS, 328, 485
Cossou C., Raymond S. N., Pierens A., 2013, A&A, 553, L2
Cox A. N., 2000, Allen's Astrophysical Quantities. Springer-Verlag, Berlin
Cresswell P., Nelson R. P., 2008, A&A, 482, 677
Crida A., Morbidelli A., 2007, MNRAS, 377, 1324
Crida A., Morbidelli A., Masset F., 2006, Icarus, 181, 587
Daisaka J. K., Tanaka H., Ida S., 2006, Icarus, 185, 492
D'Angelo G., Marzari F., 2012, ApJ, 757, 50
D'Angelo G., Kley W., Henning T., 2003, ApJ, 586, 540
Dullemond C. P., Hollenbach D., Kamp I., D'Alessio P., 2007, in Reipurth B., Jewitt D., Keil K., eds, Protostars and Planets V. Univ. Arizona Press, Tucson, AZ, p. 555
Fendyke S. M., Nelson R. P., 2014, MNRAS, 437, 96
Fogg M. J., Nelson R. P., 2007, A&A, 472, 1003
Fogg M. J., Nelson R. P., 2009, A&A, 498, 575
Forgan D., Rice K., 2013, MNRAS, 432, 3168
Gillon M. et al., 2014, A&A, 562, L3
Gressel O., Nelson R. P., Turner N. J., Ziegler U., 2013, ApJ, 779, 59
Hayashi C., 1981, Prog. Theor. Phys. Suppl., 70, 35
Hellary P., Nelson R. P., 2012, MNRAS, 419, 2737
Hubeny I., 1990, ApJ, 351, 632
Hubickyj O., Bodenheimer P., Lissauer J. J., 2005, Icarus, 179, 415
Ida S., Lin D. N. C., 2010, ApJ, 719, 810
Ida S., Lin D. N. C., Nagasawa M., 2013, ApJ, 775, 42
Inaba S., Ikoma M., 2003, A&A, 410, 711
Kasting J. F., Whitmire D. P., Reynolds R. T., 1993, Icarus, 101, 108
Kley W., 1999, MNRAS, 303, 696
Lammer H. et al., 2014, MNRAS, 439, 3225
Lin D. N. C., Papaloizou J., 1986, ApJ, 309, 846
Lissauer J. J. et al., 2011, Nature, 470, 53
Lubow S. H., Seibert M., Artymowicz P., 1999, ApJ, 526, 1001
McNeil D. S., Nelson R. P., 2009, MNRAS, 392, 537
McNeil D. S., Nelson R. P., 2010, MNRAS, 401, 1691
McNeil D., Duncan M., Levison H. F., 2005, AJ, 130, 2884
Masset F., Snellgrove M., 2001, MNRAS, 320, L55
Mayor M., Queloz D., 1995, Nature, 378, 355
Menou K., Goodman J., 2004, ApJ, 606, 520
Miguel Y., Guilera O. M., Brunini A., 2011a, MNRAS, 412, 2113
Miguel Y., Guilera O. M., Brunini A., 2011b, MNRAS, 417, 314
Morbidelli A., Tsiganis K., Crida A., Levison H. F., Gomes R., 2007, AJ, 134, 1790
Mordasini C., Alibert Y., Benz W., 2009, A&A, 501, 1139
Mordasini C., Alibert Y., Benz W., Klahr H., Henning T., 2012, A&A, 541, A97
Movshovitz N., Bodenheimer P., Podolak M., Lissauer J. J., 2010, Icarus, 209, 616
Nelson R. P., Papaloizou J. C. B., Masset F., Kley W., 2000, MNRAS, 318, 18
Paardekooper S.-J., Baruteau C., Crida A., Kley W., 2010, MNRAS, 401, 1950
Paardekooper S.-J., Baruteau C., Kley W., 2011, MNRAS, 410, 293
Papaloizou J. C. B., Larwood J. D., 2000, MNRAS, 315, 823
Papaloizou J. C. B., Nelson R. P., 2005, A&A, 433, 247
Papaloizou J. C. B., Terquem C., 1999, ApJ, 521, 823
Pierens A., Cossou C., Raymond S. N., 2013, A&A, 558, 105
Podolak M., Podolak J. I., Marley M. S., 2000, Planet. Space Sci., 48, 143
Pollack J. B., Hubickyj O., Bodenheimer P., Lissauer J. J., Podolak M., Greenzweig Y., 1996, Icarus, 124, 62
Rauer H. et al., 2013, preprint (arXiv:e-prints)
Schneider J., Dedieu C., Le Sidaner P., Savalle R., Zolotukhin I., 2011, A&A, 532, A79
Shakura N. I., Sunyaev R. A., 1973, A&A, 24, 337
Soummer R., Brendan Hagan J., Pueyo L., Thormann A., Rajan A., Marois C., 2011, ApJ, 741, 55
Szulágyi J., Morbidelli A., Crida A., Masset F., 2014, ApJ, 782, 65
Terquem C., Papaloizou J. C. B., 2007, ApJ, 654, 1110
Ziegler U., Yorke H. W., 1997, Comput. Phys. Commun., 101, 54

This paper has been typeset from a TEX/LATEX file prepared by the author.